

See discussions, stats, and author profiles for this publication at: <https://www.researchgate.net/publication/347627587>

On the Upper-Ocean Vertical Eddy Heat Transport in the Kuroshio Extension. Part I: Variability and Dynamics

Article in *Journal of Physical Oceanography* · January 2021

DOI: 10.1175/JPO-D-20-0068.1

CITATION

1

7 authors, including:



Peiran Yang

Ocean University of China

2 PUBLICATIONS 7 CITATIONS

[SEE PROFILE](#)



Bingrong Sun

Ocean University of China

6 PUBLICATIONS 7 CITATIONS

[SEE PROFILE](#)

READS

314



Zhao Jing

Texas A&M University

40 PUBLICATIONS 521 CITATIONS

[SEE PROFILE](#)



Lixin Wu

Qingdao National Laboratory for Marine Science and Technology (QNLN)

205 PUBLICATIONS 8,106 CITATIONS

[SEE PROFILE](#)

Some of the authors of this publication are also working on these related projects:



Social Enterprise [View project](#)



Synergy of current and future satellite observations [View project](#)

On the Upper-Ocean Vertical Eddy Heat Transport in the Kuroshio Extension. Part I: Variability and Dynamics

PEIRAN YANG,^{a,b} ZHAO JING,^{a,b,c} BINGRONG SUN,^{a,b} LIXIN WU,^{a,b} BO QIU,^d
PING CHANG,^{c,e,f} AND SANJIV RAMACHANDRAN^{c,e}

^a Key Laboratory of Physical Oceanography and Frontiers Science Center for Deep Ocean Multispheres and Earth System, Ocean University of China, Qingdao, China

^b Pilot National Laboratory for Marine Science and Technology (Qingdao), Qingdao, China

^c International Laboratory for High-Resolution Earth System Prediction, Texas A&M University, College Station, Texas

^d Department of Oceanography, University of Hawai'i at Mānoa, Honolulu, Hawaii

^e Department of Oceanography, Texas A&M University, College Station, Texas

^f Department of Atmospheric Sciences, Texas A&M University, College Station, Texas

(Manuscript received 30 March 2020, in final form 19 October 2020)

ABSTRACT: Oceanic eddies play a crucial role in transporting heat from the subsurface to surface ocean. However, dynamics responsible for the vertical eddy heat transport Q_T have not been systematically understood, especially in the mixed layer of western boundary current extensions characterized by the coincidence of strong eddy activities and air–sea interactions. In this paper, the winter (December–March) Q_T in the Kuroshio Extension is simulated using a 1-km regional ocean model. An omega equation based on the geostrophic momentum approximation and generalized to include the viscous and diabatic effects is derived and used to decompose the contribution of Q_T from different dynamics. The simulated Q_T exhibits a pronounced positive peak around the center of the mixed layer (~ 60 m). The value of Q_T there exhibits multi-time-scale variations with irregularly occurring extreme events superimposed on a slowly varying seasonal cycle. The proposed omega equation shows good skills in reproducing Q_T , capturing its spatial and temporal variations. Geostrophic deformation and vertical mixing of momentum are found to be the two major processes generating Q_T in the mixed layer with the former and the latter accounting for its seasonal variation and extreme events, respectively. The mixed layer instability and the net effect of frontogenesis/frontolysis contribute comparably to the geostrophic deformation induced Q_T . The contribution of Q_T from vertical mixing of momentum can be understood on the basis of turbulent thermal wind balance.

KEYWORDS: Vertical motion; Eddies; Oceanic mixed layer

1. Introduction

Oceanic eddies¹ are ubiquitous in the upper ocean. They are thought to produce intense vertical flows of $O(100)$ m day^{−1} that are instrumental in supplying heat, nutrients, and oxygen to the mixed layer and in shaping the upper-ocean thermal structures (e.g., McGillicuddy et al. 2003; Boccaletti et al. 2007; Klein and Lapeyre 2009; Mahadevan et al. 2012; Rosso et al. 2014; Yu et al. 2019). Many mechanisms for the generation of eddy vertical flows and associated heat transport in the upper ocean have been proposed. In the adiabatic and inviscid framework, the frontogenesis/frontolysis (Hoskins and Bretherton 1972; Hoskins 1982) and the mixed layer instability (Boccaletti et al. 2007; Fox-Kemper et al. 2008) are two

major processes. During frontogenesis, intensification of a front by background confluent flows induces ageostrophic secondary circulation (ASC) with upwelling and downwelling on lighter (commonly warmer) and denser (commonly colder) side of the front, respectively. The opposite occurs during frontolysis. The mixed layer instability is the type of baroclinic instability developing in the weakly stratified surface mixed layer at fronts (Boccaletti et al. 2007; Fox-Kemper et al. 2008; McWilliams 2016). The most unstable modes occur at ocean submesoscales and produce strong vertical eddy heat transport peaking within the mixed layer (Stone 1966; Boccaletti et al. 2007).

The vertical turbulent viscous effect in the mixed layer is also able to induce vertical eddy heat transport. By destroying the vertical shear of eddies, it produces an ASC with a similar pattern to that by the frontogenesis (Garrett and Loder 1981; Nagai et al. 2006; Gula et al. 2014). Moreover, intense vertical eddy motions can be induced by atmospheric forcing. Winds blowing in the downfront direction (the so-called downfront winds) result in a destabilizing buoyancy flux caused by cross-front Ekman transport and further a frontogenetic ASC through the nonlinear Ekman pumping (Thomas and Lee 2005).

Tremendous efforts have been put into seeking comprehensive understanding of contributions from the aforementioned

¹ In this study, oceanic balanced variabilities at mesoscales and submesoscales are loosely referred to as eddies.

Supplemental information related to this paper is available at the Journals Online website: <https://doi.org/10.1175/JPO-D-20-0068.s1>.

Corresponding author: Zhao Jing, jingzhao198763@sina.com

mechanisms to the upper-ocean vertical eddy heat transport in reality. Attempts based on in situ observations are challenging due to difficulties in sampling three-dimensional (3D) flow structures with sufficient resolutions and in measuring diabatic and viscous effects. Typically, some crude assumptions have to be adopted to enable estimates and, even in this case, not all the mechanisms can be evaluated jointly (Pollard and Regier 1992; Martin and Richards 2001; Naveira Garabato et al. 2001; Pallàs-Sanz and Viúdez 2005; Nagai et al. 2006; Pallàs-Sanz et al. 2010; Yu et al. 2019; Siegelman et al. 2020), making it difficult to assess their relative importance comprehensively.

High-resolution numerical simulations provide a viable alternative. Numerous studies explore this problem based on numerical models configured for various situations, ranging from idealized fronts (Thomas and Lee 2005; Lapeyre and Klein 2006; Mahadevan and Tandon 2006; Fox-Kemper et al. 2008; Thomas and Ferrari 2008) to more realistic simulations in regions with different dynamic regimes (Giordani et al. 2006; Capet et al. 2008b; Mensa et al. 2013; Zhong and Bracco 2013; Bachman and Taylor 2016; Qiu et al. 2016; Su et al. 2018; Estrada-Allis et al. 2019; Qiu et al. 2020). Although these studies significantly advance our understanding, they have two important limitations. First, most studies, not all, address the vertical velocity of eddies rather than their associated heat transport, but it is the latter that shapes the upper-ocean stratification and further affects the climate. It remains unclear to what extent these vertical eddy motions are capable of producing net heat transport. Second, a direct decomposition of vertical eddy heat transport into contributions from different mechanisms has not been achieved partially due to the lack of feasible diagnostic tools.

Western boundary current (WBC) extensions are characterized by strong eddy activities (Ducet and Le Traon 2001; von Storch et al. 2012; Chen et al. 2014; Su et al. 2018). They are also the key sites for the atmospheric heat uptake (Yu and Weller 2007; Cronin et al. 2010). By transporting heat from the subsurface to surface region, eddies in WBC extensions might be crucial for sustaining the ocean heat release there and thus exert a significant impact on the midlatitude atmosphere variability (Chelton et al. 2004; Minobe et al. 2008; Nakamura et al. 2008; Small et al. 2008; Tokinaga et al. 2009; Jing et al. 2020). However, underlying dynamics of the vertical eddy heat transport and its potential regulation by air–sea interactions in these regions have not been systematically assessed. In this first paper (i.e., Part I), we analyze the variability of vertical eddy heat transport and its underlying dynamics in the winter Kuroshio Extension using a high-resolution (~ 1 km) regional ocean simulation. An omega equation based on the geostrophic momentum approximation (GMA) (Eliassen 1949; Hoskins and Bretherton 1972; Hoskins 1975) and generalized to include the viscous and diabatic effects is formulated to isolate contributions from different dynamics. Influences of air–sea interactions on the vertical eddy heat transport will be addressed in Part II (P. Yang et al. 2020, unpublished manuscript).

This paper is structured as follows. Section 2 presents configuration of the numerical model and formulation of the omega equation. The performance of the proposed omega

equation in terms of reproducing vertical eddy velocity and associated heat transport is evaluated in section 3. A decomposition of vertical eddy heat transport into components with different dynamics is addressed in section 4, with dominant mechanisms identified. Discussion on the limitation and implication of this study is presented in section 5 followed by conclusions.

2. Data and methods

a. Regional model

The Regional Ocean Modeling System (ROMS; Haidvogel et al. 2000; Shchepetkin and McWilliams 2005) is configured over 146.6° – 168.5° E and 29° – 42.6° N (the dashed white box in Fig. 1a) to simulate eddies and their vertical heat transport in the winter Kuroshio Extension. The simulation has a horizontal resolution of ~ 1 km and 65 levels in a vertical terrain-following coordinate. The vertical grid size in the upper 100 m ranges from 4.7 to 6.0 m. A *K*-profile parameterization (KPP) turbulent mixing closure scheme is used for vertical mixing (Large et al. 1994). A biharmonic horizontal Smagorinsky-like mixing scheme (Griffies and Hallberg 2000) is used for momentum. No horizontal mixing parameterization for tracers is applied. The simulated sea surface salinity (SSS) is restored to the climatological SSS from Simple Ocean Data Assimilation (SODA; Carton et al. 2018) with a nudging time scale of 10 days.

The atmospheric forcing for the 1-km ROMS simulation is derived from the 6-hourly Climate Forecast System Reanalysis (CFSR; Saha et al. 2010). The boundary conditions are obtained from the daily averaged velocity and hydrographic records output by a ROMS simulation configured over the North Pacific (99° – 270° E, 3.6° – 66° N; Fig. 1a) with a horizontal resolution of ~ 9 km and 50 vertical levels. The mixing and restoring schemes for the 9-km ROMS simulation are the same as those in the 1-km ROMS simulation. The initial and boundary conditions for the 9-km ROMS simulation are obtained from SODA, and its atmospheric forcing is the same as the 1-km ROMS simulation.

The 9-km ROMS simulation is initialized on 1 January 1998 and integrated to 2 October 2008. Its simulation result on 30 September 2004 is used as the initial condition for the 1-km ROMS simulation. The 1-km ROMS simulation is integrated for 6 months with a 2-month spinup, outputting 3-hourly averaged 3D velocity, temperature, salinity, and individual diagnostic terms in momentum and tracer equations. The outputs from 1 December to 31 March are used for analyses. To eliminate the interference from internal gravity waves that are subject to unbalanced dynamics, all the outputs are low-pass filtered with a cutoff frequency of 0.8 the local inertial frequency.

b. Generalized omega equation

The omega equation is widely used for diagnosing vertical velocity in the ocean. It has several different formulations appropriate for different dynamical regimes (Hoskins 1982; Pinot et al. 1996; Giordani and Planton 2000; Pallàs-Sanz and Viúdez 2005; Giordani et al. 2006; Nagai et al. 2006; Pallàs-Sanz et al. 2010;

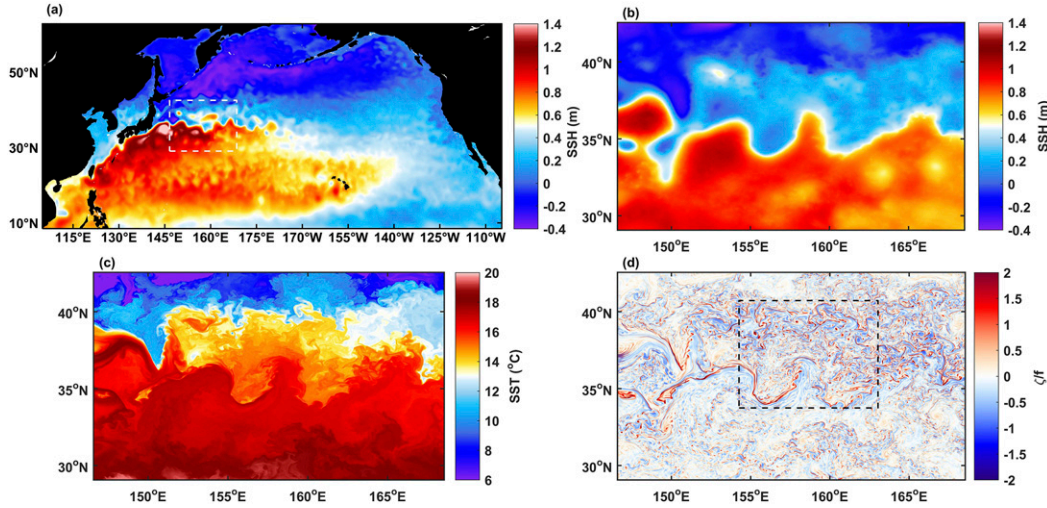


FIG. 1. Snapshots of the SSH field in the (a) 9- and (b) 1-km ROMS simulations on 21 Feb 2005. (c),(d) As in (b), but for the SST field and z/f field, respectively. The lateral boundary of the 1-km experiment is marked by the dashed lines in (a), and the G-GMA omega equation is solved in the region indicated by the box in (d).

Qiu et al. 2020). The omega equation used in this study is built largely on GMA (Eliassen 1949; Hoskins and Bretherton 1972; Hoskins 1975) that has been widely used to formulate eddy dynamics (Hoskins 1982; Cloke and Cullen 1994; Pinot et al. 1996; Viúdez 2004; Thomas and Lee 2005; Nagai et al. 2006). Decomposing the horizontal velocity $\mathbf{v} = (u, v)$ into the geostrophic component $\mathbf{v}_g = (u_g, v_g) = [-(f\rho_0)^{-1}\partial p/\partial y, (f\rho_0)^{-1}\partial p/\partial x]$ and the ageostrophic component $\mathbf{v}_a = (u_a, v_a) = (u - u_g, v - v_g)$, the GMA equations for horizontal momentum and buoyancy generalized to include adiabatic and viscous effects are

$$\frac{\partial u_g}{\partial t} + u \frac{\partial u_g}{\partial x} + v \frac{\partial u_g}{\partial y} + w \frac{\partial u_g}{\partial z} = f v_a + D_V(u) + D_H(u), \quad (1)$$

$$\frac{\partial v_g}{\partial t} + u \frac{\partial v_g}{\partial x} + v \frac{\partial v_g}{\partial y} + w \frac{\partial v_g}{\partial z} = -f u_a + D_V(v) + D_H(v), \quad (2)$$

$$\frac{\partial b}{\partial t} + u \frac{\partial b}{\partial x} + v \frac{\partial b}{\partial y} + w \frac{\partial b}{\partial z} = D_V(b), \quad (3)$$

$$\frac{\partial u_a}{\partial x} + \frac{\partial v_a}{\partial y} + \frac{\partial w}{\partial z} = 0, \quad (4)$$

where w is the vertical velocity, f the Coriolis parameter, $b = -g\rho_0^{-1}(\rho - \rho_0)$ the buoyancy with g the gravitational acceleration, ρ the potential density and ρ_0 set as 1025 kg m^{-3} , p the pressure, $D_V(u)/D_V(v)$ the vertical mixing for zonal/meridional momentum, $D_H(u)/D_H(v)$ the horizontal mixing for zonal/meridional momentum, and $D_V(b)$ the vertical mixing for buoyancy (see Table 1 for key symbols used in this paper). It should be noted that to obtain Eq. (4), we drop the term proportional to the meridional derivative of f .²

After some manipulations, we obtain the following diagnostic equation for w (see the appendix for derivation details):

$$f^2 \frac{\partial^2 w}{\partial z^2} + \nabla_H \cdot (N^2 \nabla_H w) = 2 \nabla_H \cdot \mathbf{Q} + \nabla_H \cdot \mathbf{A} - f \frac{\partial}{\partial z} \left[\frac{\partial D_V(v)}{\partial x} - \frac{\partial D_V(u)}{\partial y} \right] - f \frac{\partial}{\partial z} \left[\frac{\partial D_H(v)}{\partial x} - \frac{\partial D_H(u)}{\partial y} \right] + \nabla_H^2 [D_V(b)], \quad (5)$$

with

$$\mathbf{Q} = - \left(\frac{\partial \mathbf{v}_g}{\partial x} \cdot \nabla_H b, \frac{\partial \mathbf{v}_g}{\partial y} \cdot \nabla_H b \right), \quad (6)$$

$$\mathbf{A} = \left(f \frac{\partial \mathbf{v}_a}{\partial z} \cdot \nabla_H v_g - f \frac{\partial \mathbf{v}_g}{\partial z} \cdot \nabla_H v_a - 2 \frac{\partial \mathbf{v}_a}{\partial x} \cdot \nabla_H b, -f \frac{\partial \mathbf{v}_a}{\partial z} \cdot \nabla_H u_g + f \frac{\partial \mathbf{v}_g}{\partial z} \cdot \nabla_H u_a - 2 \frac{\partial \mathbf{v}_a}{\partial y} \cdot \nabla_H b \right), \quad (7)$$

where $\nabla_H = (\partial/\partial x, \partial/\partial y)$ and $N^2 = \partial b/\partial z$ is the squared buoyancy frequency.

We make further simplification to the differential operator on the lhs of Eq. (5) by replacing N^2 in $\nabla_H \cdot (N^2 \nabla_H w)$ with its horizontal average $\langle N^2 \rangle_s$ ($\langle \cdot \rangle_s$ denotes the spatial average in the

² This is not equivalent to setting f as a single value. Instead, we treat f as a slowly varying parameter with terms proportional to its meridional derivative neglected.

TABLE 1. Key symbols used in this paper.

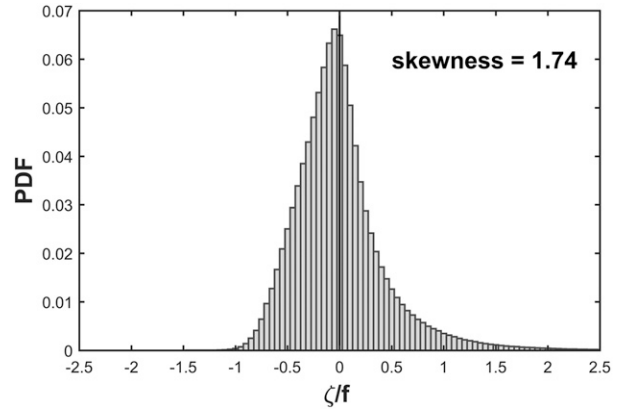
Symbol	Name
\mathbf{v}_g	Geostrophic velocity, (u_g, v_g)
\mathbf{v}_a	Horizontal ageostrophic velocity, (u_a, v_a)
w, w^o	Vertical velocity, vertical velocity estimated from G-GMA omega equation
b	Buoyancy
f	Coriolis parameter
H	Mixed layer depth
∇_H	$\nabla_H = (\partial/\partial x, \partial/\partial y)$
Q_T	Vertical eddy heat transport
B_f	Vertical eddy buoyancy flux
A^o	Any variable A derived based on w^o
$\langle A \rangle_s$	Horizontal average of A
$\langle A \rangle_{s,t}$	Temporal and horizontal average of A
A^z	Vertical average of A within the mixed layer
\bar{A}	Spatial smoothing of A
\mathbf{n}	Unit vector in the cross-front direction determined by $\nabla \bar{b}^z$
M	$(\bar{H} \nabla \bar{b}^z)^2$
Π	Cross-front confluence by ambient flows, $-(\partial \bar{u}_{gn}/\partial n)^z$
$A\{M, \Pi\}$	Bin averaged A with respect to M and Π

horizontal domain hereinafter). Such simplification makes no noticeable difference to the vertical eddy heat transport estimated from the omega equation (Fig. A1), but facilitates computation and interpretation of the solution. Applying the aforementioned simplification to Eq. (5) yields

$$f^2 \frac{\partial^2 w}{\partial z^2} + \langle N^2 \rangle_s \nabla_H^2 w = 2 \nabla_H \cdot \mathbf{Q} + \nabla_H \cdot \mathbf{A} - f \frac{\partial}{\partial z} \left[\frac{\partial D_V(v)}{\partial x} - \frac{\partial D_V(u)}{\partial y} \right] - f \frac{\partial}{\partial z} \left[\frac{\partial D_H(v)}{\partial x} - \frac{\partial D_H(u)}{\partial y} \right] + \nabla_H^2 [D_V(b)]. \quad (8)$$

Equation (8) together with Eqs. (6) and (7) forms the diagnostic tool for vertical eddy velocity and associated heat transport in this study. It generalizes the GMA omega equation proposed by Pinot et al. (1996) with viscous and diabatic effects included. For this sake, we refer to it as the generalized GMA (G-GMA) omega equation hereinafter. The G-GMA omega equation can also be treated as a reduced version of the omega equation for the primitive equation system (Giordani and Planton 2000; Giordani et al. 2006). By approximating the advected momentum by its geostrophic value, it filters out internal gravity waves that are known to produce strong vertical velocity but little vertical heat transport (Hoskins 1975; Alford et al. 2016).

The first term on the rhs of Eq. (8) corresponds to the geostrophic deformation. Equation (8) is reduced to the classical quasigeostrophic (QG) omega equation (Hoskins 1982) when only this term is present on the rhs. The second term corresponds to the effect of higher-order dynamics (i.e., ageostrophic advection effect) in the GMA regime. Effects of vertical mixing of momentum, horizontal mixing of momentum, and vertical mixing of buoyancy are included sequentially in the third, fourth and last terms. Due to the linear nature of

FIG. 2. The probability density function (PDF) of s/f with its skewness shown in text.

Eq. (8), its solution, w^o , can be represented as the superposition of six independent components with distinct dynamics, i.e.,

$$w^o = w^{qg} + w^{ag} + w^{vm} + w^{hm} + w^{vb} + w^{bry}. \quad (9)$$

The solutions w^{qg} , w^{ag} , w^{vm} , w^{hm} , and w^{vb} represent contributions from individual rhs forcing terms, solved by only keeping the corresponding forcing term and setting $w = 0$ on the boundaries. The solution w^{bry} represents contribution from the boundary conditions and is obtained by dropping all the forcing terms but using the model output as boundary conditions of w . The G-GMA omega equation is solved over the domain 154.3°–163.0°E, 33.7°–40.7°N (800 km \times 780 km or so, as in Fig. 1d), and 0–530 m in depth using successive overrelaxation method with Chebyshev acceleration (Press et al. 1992; Allen et al. 2001). This computational domain is far away from the lateral boundaries of the 1-km ROMS simulation and much larger than the size of eddies dominating the vertical eddy heat transport (Capet et al. 2008b; Klein and Lapeyre 2009; Su et al. 2018; Yu et al. 2019; Siegelman et al. 2020).

3. Evaluation of the performance of G-GMA omega equation

Figures 1b–d display snapshots of sea surface height (SSH), sea surface temperature (SST) and vertical relative vorticity ς on 21 February 2005 for the 1-km ROMS simulation, along with a snapshot of SSH in the parent 9-km ROMS simulation on the same day (Fig. 1a). Strong eddy activities occur in the SST frontal regions, as evidenced by the large values of ς there. Consistent with previous simulation studies of similar horizontal resolutions, the probability density function (PDF) of s/f is characterized by a positive skewness (Fig. 2), implying an active role of ageostrophic advections in our simulation (Rudnick 2001; Shcherbina et al. 2013).

The G-GMA omega equation exhibits moderate skills in reproducing w in the upper ocean. The temporal and spatial variabilities of w^o mimic those of w (Figs. 3a,b and 4a,c). However, w^o is significantly lower in magnitude than w below 70 m (Fig. 4c). For instance, the time mean $\langle w^{o2} \rangle_s$ (denoted as

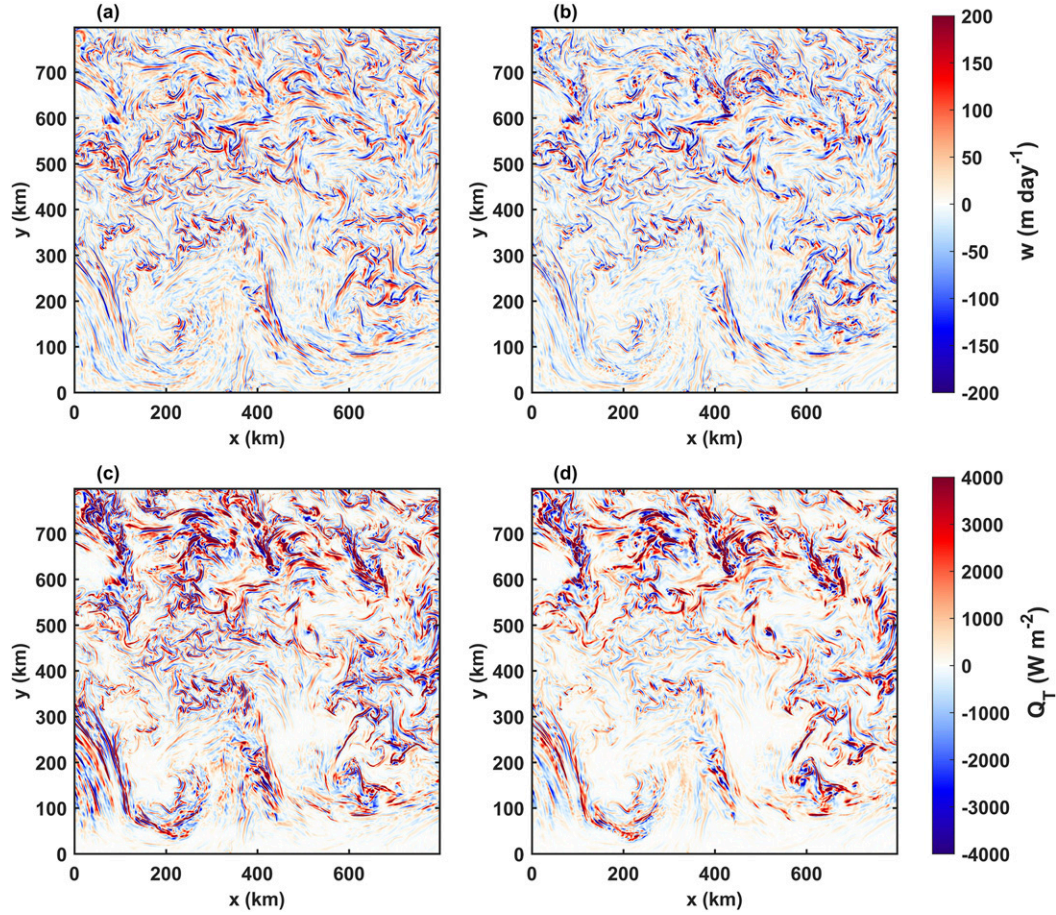


FIG. 3. Snapshots of (a) w , (b) w^o at 90 m, (c) Q_T , and (d) Q_T^o at 60 m on 21 Feb 2005.

$\langle w^{o2} \rangle_{s,t}$ henceforth) is only 41% of $\langle w^2 \rangle_{s,t}$ at 90 m. The smaller magnitude of $\langle w^{o2} \rangle_{s,t}$ than $\langle w^2 \rangle_{s,t}$ might be partially due to the negligence of the material derivative of ageostrophic flows by GMA. In fact, we find that the magnitudes of material derivatives of geostrophic and ageostrophic flows are of the same order (not shown).

We next examine the performance of G-GMA in reproducing the vertical eddy heat transport Q_T computed as

$$Q_T = \rho_0 c_p w' T',$$

where T is the temperature, c_p is the seawater specific heat capacity, and the prime represents eddy anomalies defined as perturbations from zonal average. We approximate w' by w to facilitate the dynamical analysis in section 4. This approximation will not affect the regional mean results, i.e., $\langle Q_T \rangle_s$. Moreover, it is found that the spatial patterns of $\rho_0 c_p w T'$ and $\rho_0 c_p w' T'$ are almost identical due to the smallness of zonal mean w . Their pattern correlation coefficient is more than 0.96 in the upper 500 m throughout the simulation period.

In contrast to w , Q_T is well reproduced by the G-GMA omega equation. The horizontal patterns of Q_T and that estimated from the G-GMA omega equation (Q_T^o) resemble each other, both exhibiting large positive values along the

SST fronts (Figs. 3c,d). The vertical distribution of $\langle Q_T \rangle_{s,t}$ is characterized by a dipolar structure (Fig. 4d). Similar to the existing studies (Fox-Kemper et al. 2008; Ramachandran et al. 2014; Capet et al. 2016), there is a strong positive peak ($\sim 126 \text{ W m}^{-2}$) around the center of the mixed layer ($\sim 60 \text{ m}$), corresponding to a restratification flux associated with the conversion from eddy potential energy (EPE) to eddy kinetic energy (EKE). The weak negative peak of $\langle Q_T \rangle_{s,t}$ below 240 m implies that eddies in the permanent thermocline of the downstream Kuroshio Extension act to maintain the mean flow there, consistent with the findings by Waterman and Jayne (2011). The vertical profile of $\langle Q_T^o \rangle_{s,t}$ agrees remarkably well with that of $\langle Q_T \rangle_{s,t}$. Their difference is less than 5 W m^{-2} throughout the upper 500 m.

The temporal variability of $\langle Q_T \rangle_s$ is also reproduced by the G-GMA omega equation at a high level of accuracy. For instance, $\langle Q_T \rangle_s$ at 60 m exhibits multiscale variations with irregularly occurring extreme events superimposed on a slowly varying seasonal cycle. Such features are well replicated by $\langle Q_T^o \rangle_s$, with the correlation coefficient between the two time series reaching up to 0.98 (Fig. 4b).

The different performances of the G-GMA omega equation in reproducing $\langle w^2 \rangle_{s,t}$ and $\langle Q_T \rangle_{s,t}$ imply that not all vertical eddy motions make net contribution to the heat transport averaged

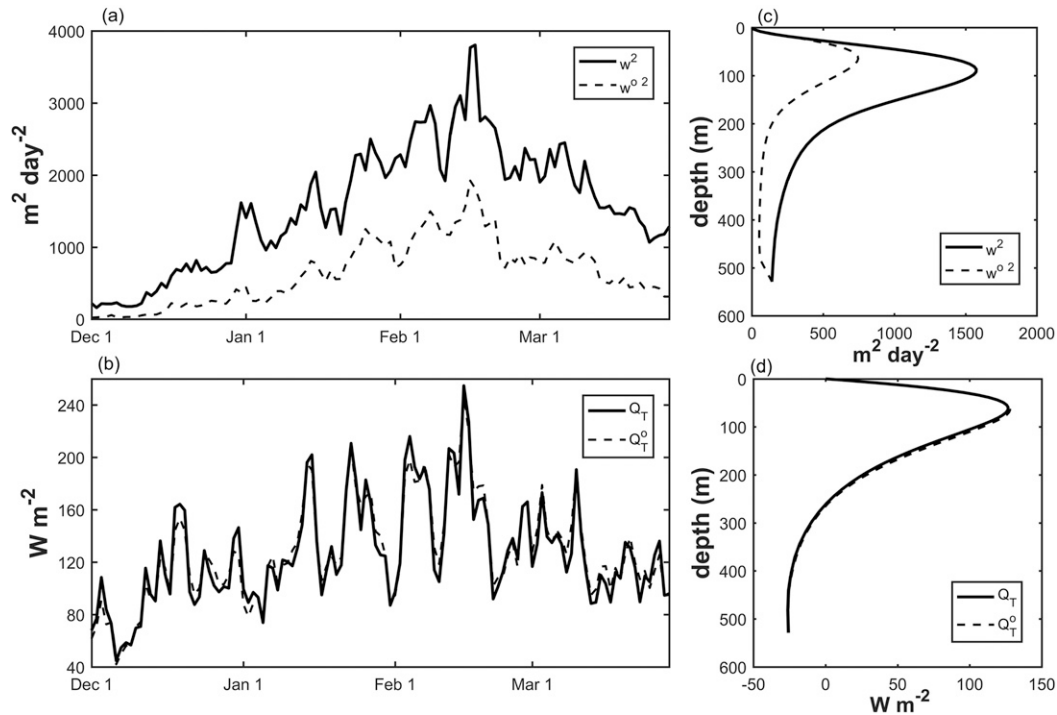


FIG. 4. (a) Time series of $\langle w^2 \rangle_s$ (solid) and $\langle w^{\circ 2} \rangle_s$ (dashed) at the peaking depth (90 m) of the former. (b) As in (a), but for $\langle Q_T \rangle_s$ (solid) and $\langle Q_T^o \rangle_s$ (dashed) at the peaking depth (60 m). (c), (d) Vertical profiles of time-mean variables shown in (a) and (b).

over time and/or space. This is confirmed by the low-to-moderate spectral correlation (the real part of coherence) between w and T' (Fig. 5). Its value in the upper 500 m is less than 0.6 throughout horizontal wavenumbers. The vertical eddy motions related to the material derivative of ageostrophic flows but unaccounted for by the G-GMA omega equation are thus likely to contribute little to $\langle Q_T \rangle_{s,t}$. More insight into this issue might be gained by using an omega equation for the primitive equation system (Giordani et al. 2006; Qiu et al. 2020) but will not be pursued in this study. Nevertheless, the good agreement between Q_T and Q_T^o gives us confidence that the G-GMA omega equation proposed in this study serves as a reliable tool for disentangling the underlying dynamics for vertical eddy heat transport in the upper ocean.

4. Mechanisms dominating the vertical eddy heat transport in the upper ocean

In this section, the relative importance of individual mechanisms for the vertical eddy heat transport is evaluated. We will focus on the mixed layer region where the vertical eddy heat transport is strongest and its influence on the atmosphere is most prominent. As it is the density or buoyancy instead of temperature that directly affects the motions of fluids, we will use the vertical eddy buoyancy flux ($B_f = wb'$) as a proxy for Q_T to facilitate the dynamical analysis. In fact, the buoyancy change is dominated by the temperature change in our computational domain so that the vertical distributions and temporal variations of Q_T and B_f resemble each other (Figs. 4 and 6).

As can be expected, the G-GMA omega equation reproduces B_f as well as Q_T (Figs. 6a,c).

a. Contribution to the $\langle B_f \rangle_{s,t}$

The decomposition of w^o into different components reveals that w^{ag} and w^{vm} make dominant contributions to $\langle B_f \rangle_{s,t}$ in the mixed layer. The vertical profile of $\langle B_f^{ag} + B_f^{vm} \rangle_{s,t}$ is close to that of $\langle B_f \rangle_{s,t}$ (Fig. 6d), with their peak values differing by less than 13%.

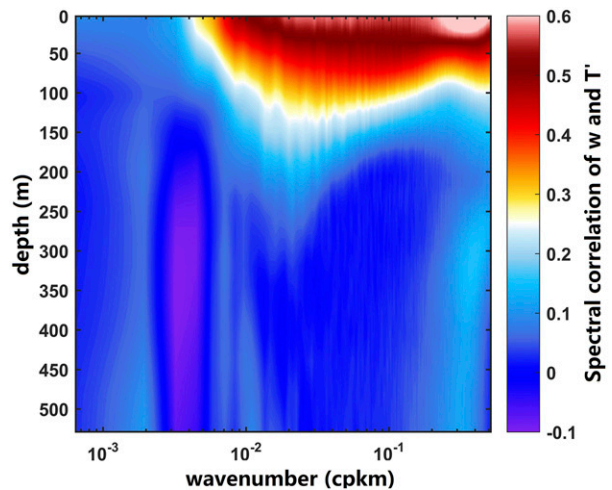


FIG. 5. Spectral correlation of w and T' as a function of horizontal wavenumber and depth.

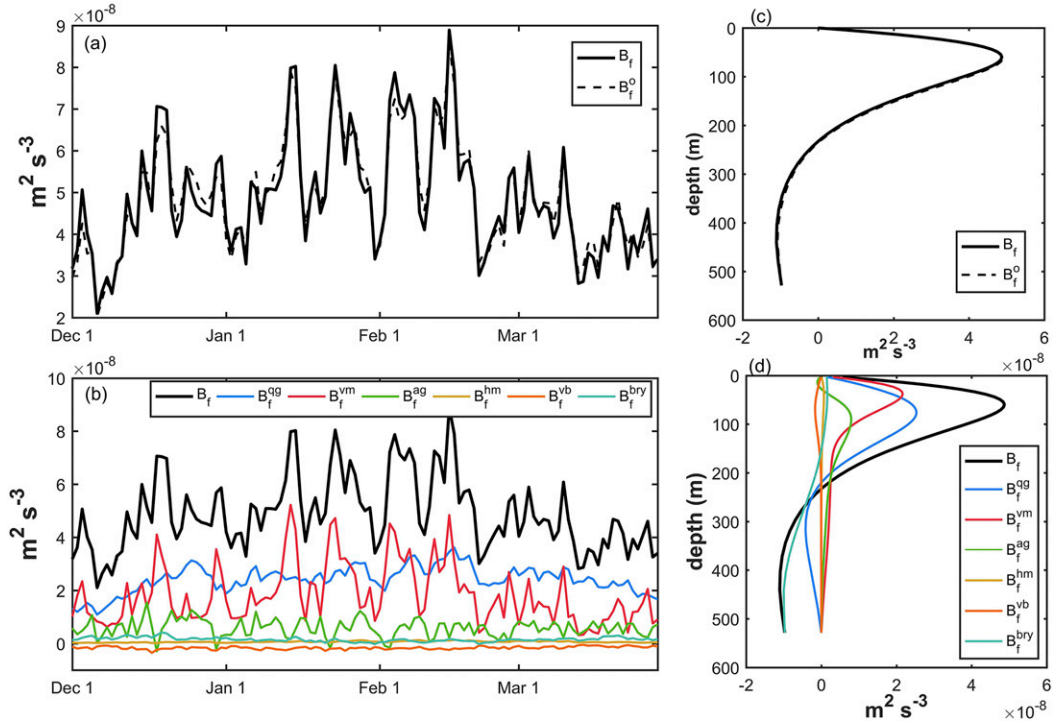


FIG. 6. (a) Time series of $\langle B_f \rangle_s$ (solid) and $\langle B_f^o \rangle_s$ (dashed) at 60 m. (b) Time series of $\langle B_f^{ag} \rangle_s$ (blue), $\langle B_f^{vm} \rangle_s$ (red), $\langle B_f^{ag} \rangle_s$ (green), $\langle B_f^{hm} \rangle_s$ (yellow), $\langle B_f^{vb} \rangle_s$ (orange), and $\langle B_f^{bry} \rangle_s$ (cyan) at 60 m. (c),(d) Vertical profiles of time-mean variables shown in (a) and (b).

The distribution of $\langle B_f^{ag} \rangle_{s,t}$ is characterized by a broad peak around 75 m. In contrast, $\langle B_f^{vm} \rangle_{s,t}$ has a much shallower structure with its value peaking around 40 m and becoming negligible below the mixed layer, as can be expected from the much weakened turbulent mixing in the thermocline.

Contribution to $\langle B_f \rangle_{s,t}$ by w^{ag} , $\langle B_f^{ag} \rangle_{s,t}$, has a dipolar vertical structure with a narrow negative peak around 13 m and a broad positive peak around 90 m (Fig. 6d). The magnitudes of its shallow and deep peaks are respectively much smaller than those of $\langle B_f^{vm} \rangle_{s,t}$ and $\langle B_f^{ag} \rangle_{s,t}$, making its contribution to $\langle B_f \rangle_{s,t}$ secondary. The effects of the boundary conditions $\langle B_f^{bry} \rangle_{s,t}$, horizontal mixing of momentum $\langle B_f^{hm} \rangle_{s,t}$, and vertical mixing of buoyancy $\langle B_f^{vb} \rangle_{s,t}$ are even smaller and can be neglected in the upper ocean.

b. Contribution to the temporal variability of $\langle B_f \rangle_s$

The temporal variability of $\langle B_f \rangle_s$ is also dominated by $\langle B_f^{ag} \rangle_s$ and $\langle B_f^{vm} \rangle_s$ with the correlation coefficient between the time series of $\langle B_f \rangle_s$ and $\langle B_f^{ag} + B_f^{vm} \rangle_s$ reaching up to 0.95 at 60 m (Fig. 6b). It should be noted that the temporal variations of $\langle B_f^{ag} \rangle_s$ and $\langle B_f^{vm} \rangle_s$ are distinct from each other with their correlation coefficient less than 0.34 at 60 m. The former is dominated by a seasonal cycle peaking around February, which largely explains the variation of $\langle B_f \rangle_s$ at seasonal time scales. The latter is characterized by irregularly occurring extreme events that account for the intraseasonal variations of $\langle B_f \rangle_s$.

The time series of $\langle B_f^{ag} \rangle_s$ at 60 m generally follows that of $\langle B_f^{ag} \rangle_s$. But the magnitude of $\langle B_f^{ag} \rangle_s$ is considerably smaller

(Figs. 6b,d). It thus suggests that the ageostrophic advection effect is not fundamental to the vertical eddy buoyancy flux but instead results in a minor modification of solutions derived from the QG regime, which seems to be consistent with the findings in previous theoretical studies (e.g., Stone 1970; Boccaletti et al. 2007). The temporal variations of $\langle B_f^{hm} \rangle_s$, $\langle B_f^{vb} \rangle_s$ and $\langle B_f^{bry} \rangle_s$ are insignificant and contribute little to that of $\langle B_f \rangle_s$.

c. Mixed layer instability versus frontogenesis/frontolysis

The mixed layer instability and the net effect of frontogenesis/frontolysis are the two candidates that may account for the positive $\langle B_f^{ag} \rangle_s$ in the mixed layer. We first examine contribution from the mixed layer instability of which the important role in generating upward buoyancy flux has been well recognized in the existing literature (Boccaletti et al. 2007; Fox-Kemper et al. 2008; Mensa et al. 2013; Callies et al. 2015; Callies and Ferrari 2018a). To do so, $\langle B_f^{ag} \rangle_s$ is compared to that derived from the parameterization of mixed layer instability proposed by Fox-Kemper et al. (2008), i.e.,

$$B_f^{FK08} = \frac{1}{f} C_e \tilde{H}^2 (\nabla_H \tilde{b}^z)^2, \quad (10)$$

where H is the mixed layer depth, the tilde represents the spatial smoothing that filters out perturbations generated by the mixed layer instability, superscript z denotes the vertical average within the mixed layer, and C_e is an empirical constant.

Based on the inviscid and adiabatic linear theories (Stone 1970), the characteristic horizontal wavelength of mixed layer instability waves can be roughly estimated as $2\pi NH/f$ assuming an $O(1)$ Richardson number and ranges from 6 to 17 km in our simulations. Therefore, a $10\text{ km} \times 10\text{ km}$ running mean with a cutoff wavelength of 20 km or so is used for spatial smoothing. Given the large uncertainties in the estimation of the horizontal wavelength of mixed layer instability waves, sensitivity tests with different filters are performed. It is found that changing the size of running mean from $6\text{ km} \times 6\text{ km}$ to $16\text{ km} \times 16\text{ km}$ does not lead to any substantial impacts on the following results (Fig. 7).

The value of C_e is chosen 0.06 as proposed by Fox-Kemper et al. (2008), whereas recent numerical simulation studies (Ramachandran et al. 2014; Callies and Ferrari 2018b) suggest that the value of C_e could be as large as 1. To get rid of the influence of large uncertainties in C_e , we focus on the temporal variability of $\langle B_f^{\text{qs}} \rangle_s$ and $\langle B_f^{\text{FK08}} \rangle_s$ rather than their time-mean magnitudes. Figure 7 displays the time series of $\langle B_f^{\text{qs}} \rangle_s$ and $\langle B_f^{\text{FK08}} \rangle_s$ at 75 m where the latter peaks. Their temporal variations differ evidently from each other with a correlation coefficient of 0.61. In particular, it is not uncommon that a local maximum (minimum) of $\langle B_f^{\text{qs}} \rangle_s$ corresponds to a local minimum (maximum) of $\langle B_f^{\text{FK08}} \rangle_s$. We note that Eq. (10) is developed based on a spindown front (Fox-Kemper et al. 2008), whereas the fronts in our simulation are continuously forced, so that Eq. (10) might not be a quantitatively reliable representation of vertical eddy buoyancy flux produced by the mixed layer instability in our simulation. Moreover, the significant discrepancy between $\langle B_f^{\text{FK08}} \rangle_s$ and $\langle B_f^{\text{qs}} \rangle_s$ suggests that the mixed layer instability is unlikely to solely account for B_f^{qs} . We suspect that the frontogenesis/frontolysis may also play an important role.

To test our conjecture, the contributions of B_f^{qs} from frontogenesis/frontolysis (denoted as B_f^{FS}) and mixed layer instability (denoted as B_f^{MLI}) are isolated based on the following procedures. We first evaluate the joint dependence of B_f^{qs} on $M = (\tilde{H}\nabla_H \tilde{b}^z)^2$ and the cross-front confluence by the ambient flows defined as $\Pi = -(\partial \tilde{u}_{g,n}/\partial n)^z$,³ where \mathbf{n} is the unit vector in the cross-front direction determined by $\nabla_H \tilde{b}^z$ (the spatial filter is used to get rid of interference from buoyancy perturbations generated by the mixed layer instability), and $\tilde{u}_{g,n}$ is the component of the smoothed geostrophic flow in the direction of \mathbf{n} . This is done by computing the bin averaged B_f^{qs} with respect to M and Π (denoted as $B_f^{\text{qs}}\{M, \Pi\}$ with the value of an argument corresponding to the center of individual bins). The value of $\langle B_f^{\text{qs}} \rangle_{s,t}$ can be linked to $B_f^{\text{qs}}\{M, \Pi\}$ according to the following equation:

$$\langle B_f^{\text{qs}} \rangle_{s,t} = \sum \sum B_f^{\text{qs}}\{M, \Pi\} P\{M, \Pi\} \Delta M \Delta \Pi, \quad (11)$$

where ΔM and $\Delta \Pi$ represent the bin sizes for M and Π , and $P\{M, \Pi\}$ represents the PDF for individual bins. Values of ΔM and $\Delta \Pi$ are not set constant but increase with the increment of M and $|\Pi|$, respectively, to ensure that there are sufficient

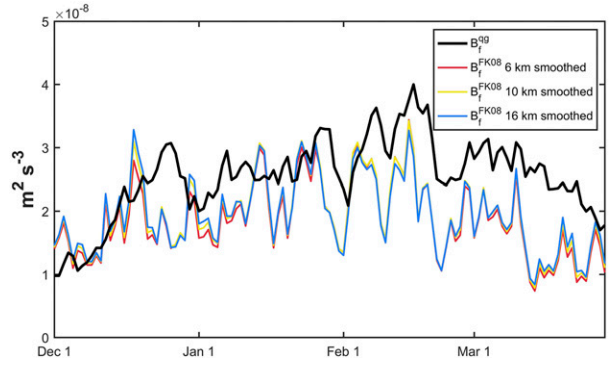


FIG. 7. Time series of $\langle B_f^{\text{qs}} \rangle_s$ (black) at its peaking depth (75 m) and $\langle B_f^{\text{FK08}} \rangle_s$ with \tilde{b} obtained by using a $6\text{ km} \times 6\text{ km}$ (red), $10\text{ km} \times 10\text{ km}$ (yellow), and $16\text{ km} \times 16\text{ km}$ (blue) running mean. Scaling factors are applied to the results with $6\text{ km} \times 6\text{ km}$ and $16\text{ km} \times 16\text{ km}$ running mean to account for the difference in $\langle (\nabla_H \tilde{b}^z)^2 \rangle_{s,t}$ among the three filters.

samples to compute the statistics for bins with large values of M and $|\Pi|$.

The core ingredient for frontogenesis/frontolysis is the nonzero value of Π (Hoskins 1982; McWilliams 2016), whereas the mixed layer instability is largely independent of Π conditional on given values of M (Fox-Kemper et al. 2008; McWilliams et al. 2009). Therefore, $B_f^{\text{FS}}\{M, \Pi\}$ and $B_f^{\text{MLI}}\{M\}$ can be respectively evaluated as

$$B_f^{\text{MLI}}\{M\} = B_f^{\text{qs}}\{M, 0\}, \quad (12)$$

$$B_f^{\text{FS}}\{M, \Pi\} = B_f^{\text{qs}}\{M, \Pi\} - B_f^{\text{qs}}\{M, 0\}. \quad (13)$$

Similar to $\langle B_f^{\text{qs}} \rangle_{s,t}$, the values of $\langle B_f^{\text{FS}} \rangle_{s,t}$ and $\langle B_f^{\text{MLI}} \rangle_{s,t}$ can be obtained as

$$\langle B_f^{\text{FS}} \rangle_{s,t} = \sum \sum B_f^{\text{FS}}\{M, \Pi\} P\{M, \Pi\} \Delta M \Delta \Pi, \quad (14)$$

$$\langle B_f^{\text{MLI}} \rangle_{s,t} = \sum B_f^{\text{MLI}}\{M\} P\{M\} \Delta M, \quad (15)$$

where $P\{M\} = \sum P\{M, \Pi\} \Delta \Pi$. It should be noted that based on Eqs. (11)–(15), we have $\langle B_f^{\text{qs}} \rangle_{s,t} = \langle B_f^{\text{MLI}} \rangle_{s,t} + \langle B_f^{\text{FS}} \rangle_{s,t}$, a decomposition of $\langle B_f^{\text{qs}} \rangle_{s,t}$ into contributions from the mixed layer instability and net effect of frontogenesis/frontolysis.

Figures 8 and 9 display the values of $B_f^{\text{qs}}\{M, \Pi\}$, $B_f^{\text{FS}}\{M, \Pi\}$, and $B_f^{\text{MLI}}\{M\}$ at the peaking depth of $\langle B_f^{\text{qs}} \rangle_{s,t}$ as well as their associated PDFs. The value of $B_f^{\text{MLI}}\{M\}$ increases monotonically with M , as expected from the mixed layer instability theory (Fox-Kemper et al. 2008; McWilliams 2016). The increase rate is approximately linear for M ranging from 2×10^{-11} to $5 \times 10^{-10} \text{ m}^2 \text{ s}^{-4}$ that more than 95% of samples are within (Fig. 9). As to $B_f^{\text{FS}}\{M, \Pi\}$, it exhibits a roughly antisymmetric pattern with respect to Π , becoming positive and negative for $\Pi > 0$ and $\Pi < 0$, respectively. The magnitude of $B_f^{\text{FS}}\{M, \Pi\}$ exhibits an increasing trend both with M and $|\Pi|$. Such features are consistent with the upward and downward eddy buoyancy flux induced by frontogenesis and frontolysis, respectively (McWilliams 2016). The above results thus support that $B_f^{\text{FS}}\{M, \Pi\}$ and $B_f^{\text{MLI}}\{M\}$ provide reliable representation of vertical eddy

³ The term M is the initial for front and Π is the initial for convergence in Greek.

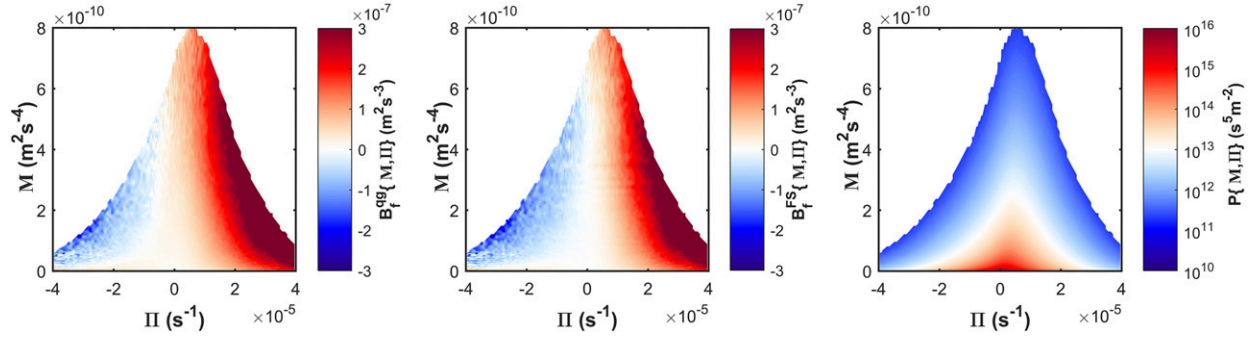


FIG. 8. Distribution of (a) $B_f^{qs}\{M, \Pi\}$, (b) $B_f^{FS}\{M, \Pi\}$, and (c) $P\{M, \Pi\}$. Bins with $P\{M, \Pi\} < 10^{11} \text{ s}^5 \text{ m}^{-2}$ are not shown as there are insufficient samples to obtain robust statistics for $B_f^{qs}\{M, \Pi\}$. Nevertheless, discarding these bins in Eqs. (11) and (14) reduces the value of $\langle B_f^{qs} \rangle_{s,t}$ and $\langle B_f^{FS} \rangle_{s,t}$ by less than 1%.

buoyancy flux induced by the frontogenesis/frontolysis and mixed layer instability. Combination of $B_f^{qs}\{M, \Pi\}$ and $B_f^{MLI}\{M\}$ causes evident asymmetry in $B_f^{qs}\{M, \Pi\}$. When $\Pi > 0$, the frontogenesis and the mixed layer instability work in concert to provide upward eddy buoyancy flux, whereas contrary contributions of the frontolysis and mixed layer instability to vertical eddy buoyancy flux compete against each other for $\Pi < 0$. In particular, for a wide range of M and Π values, the effect of mixed layer instability overcomes that of frontolysis and results in upward eddy buoyancy flux in the frontolytical regime.

Decomposition of $\langle B_f^{qs} \rangle_{s,t}$ into $\langle B_f^{FS} \rangle_{s,t}$ and $\langle B_f^{MLI} \rangle_{s,t}$ reveals that the net effect of frontogenesis/frontolysis and mixed layer instability make comparable contributions to the vertical eddy buoyancy flux induced by the geostrophic deformation in the mixed layer (Fig. 10a). The former and the latter account for 59.6% and 40.4% of the peak value of $\langle B_f^{qs} \rangle_{s,t}$ at 75 m, respectively. Again, sensitivity tests suggest that using different spatial filters to obtain \tilde{b} and $\tilde{u}_{g,n}$ does not change the results qualitatively (Fig. S1 in the online supplemental material).

It should be noted that the upward and downward eddy buoyancy fluxes induced by the frontogenesis and frontolysis tend to cancel each other, in terms of their spatial and/or temporal average. The positive $\langle B_f^{FS} \rangle_{s,t}$ in the mixed layer thus implies that the effect of frontogenesis dominates that of frontolysis, consistent with a forward cascade of EPE for geostrophic flows (Salmon 1980; Ferrari and Wunsch 2009). The dominance of frontogenesis over frontolysis could be attributed to the higher efficiency⁴ of frontogenesis than frontolysis in generating vertical eddy buoyancy flux and/or the more frequent occurrence of frontogenesis than frontolysis. Their relative importance can be assessed based on the following equation:

$$\langle B_f^{FS} \rangle_{s,t} = \sum \sum B_{f,S}^{FS} P_S \Delta M \Delta \Pi + \sum \sum B_{f,A}^{FS} P_A \Delta M \Delta \Pi, \quad (16)$$

with

$$B_{f,S}^{FS} = \frac{1}{2} B_f^{FS}\{M, \Pi\} + \frac{1}{2} B_f^{FS}\{M, -\Pi\},$$

⁴ Here a higher efficiency means larger $|B_f^{FS}|$ for given values of $|\Pi|$ and M .

$$B_{f,A}^{FS} = \frac{1}{2} B_f^{FS}\{M, \Pi\} - \frac{1}{2} B_f^{FS}\{M, -\Pi\},$$

$$P_S = \frac{1}{2} P\{M, \Pi\} + \frac{1}{2} P\{M, -\Pi\},$$

$$P_A = \frac{1}{2} P\{M, \Pi\} - \frac{1}{2} P\{M, -\Pi\},$$

where the subscripts S and A represent the symmetric and antisymmetric parts, respectively. The arguments in $B_{f,S}^{FS}$, $B_{f,A}^{FS}$, P_S , and P_A are dropped here for neatness. The first term on the rhs of Eq. (16) results from the efficiency difference between frontogenesis and frontolysis in generating vertical eddy buoyancy flux and would disappear if there were no efficiency difference. The second term is related to the difference in the occurrence frequency between frontogenesis and frontolysis and would disappear if there is no preference for their occurrence. As displayed in Fig. 10b, both the differences in efficiency and occurrence frequency contribute to the positive $\langle B_f^{FS} \rangle_{s,t}$ but the former is somewhat more dominant, accounting for around 60% of the peak value of $\langle B_f^{FS} \rangle_{s,t}$ at 75 m.

d. Dynamics for B_f^{vm}

We find that the underlying dynamics for B_f^{vm} can be understood based on the turbulent thermal wind (TTW) balance (Gula et al. 2014), i.e.,

$$f v_a = -\frac{\partial}{\partial z} \left(K_m \frac{\partial u}{\partial z} \right), \quad (17)$$

$$f u_a = \frac{\partial}{\partial z} \left(K_m \frac{\partial v}{\partial z} \right), \quad (18)$$

where K_m is the vertical mixing coefficient for momentum. Adopting the rigid-lid approximation at the sea surface as the boundary condition for TTW balance, the associated vertical velocity w^{TTW} can be derived as

$$w^{\text{TTW}} = \frac{1}{f} \left[\frac{1}{\rho_0} \nabla_H \times \boldsymbol{\tau} \cdot \mathbf{k} - \left(\frac{\partial}{\partial x} K_m \frac{\partial v}{\partial z} - \frac{\partial}{\partial y} K_m \frac{\partial u}{\partial z} \right) \right], \quad (19)$$

where $\boldsymbol{\tau}$ is the surface wind stress, and \mathbf{k} the unit vector in the z direction.

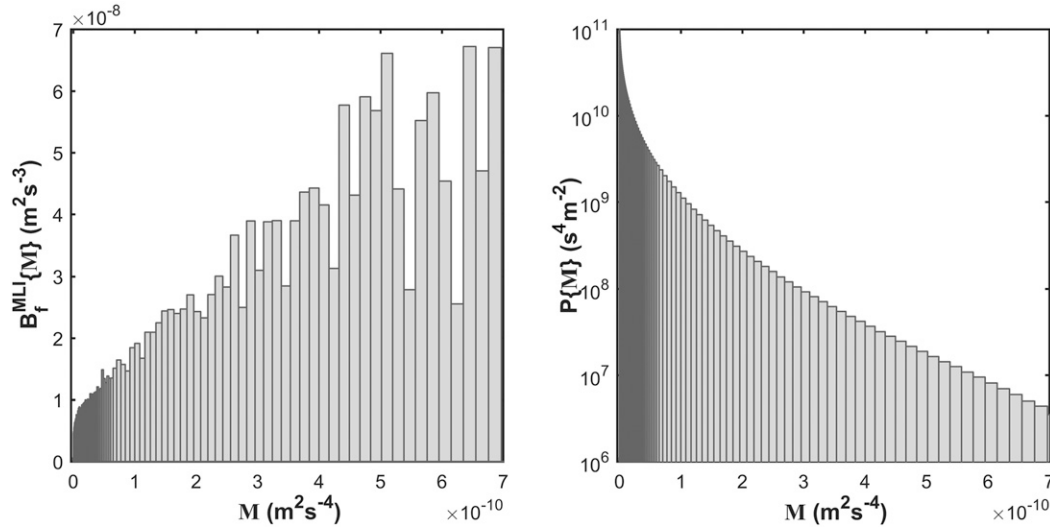


FIG. 9. Distribution of (a) $B_f^{\text{MLI}}\{M\}$ and (b) $P\{M\}$. The bar width measures the bin size ΔM . Bins with $P\{M, \Pi\} < 10^{11} \text{ s}^4 \text{ m}^{-2}$ are not shown as there are insufficient samples to obtain robust statistics for $B_f^{\text{MLI}}\{M\}$. Nevertheless, discarding these bins in Eq. (15) reduces the value of $\langle B_f^{\text{MLI}} \rangle_{s,t}$ by less than 1%.

Figures 11a and 11d compare the vertical eddy buoyancy flux estimated based on Eq. (19), i.e., $\langle B_f^{\text{TTW}} \rangle_s = \langle w^{\text{TTW}} b' \rangle_s$, to $\langle B_f^{\text{vm}} \rangle_s$. The vertical profiles of $\langle B_f^{\text{TTW}} \rangle_{s,t}$ and $\langle B_f^{\text{vm}} \rangle_{s,t}$ agree well with each other in the mixed layer (Fig. 11d). Both peak around 40 m with the magnitudes of their peaks differing by less than 8%. There is also a high similarity in their temporal variations with the correlation coefficient between their time series at 40 m above 0.99 (Fig. 11a). Below 150 m, $\langle B_f^{\text{vm}} \rangle_{s,t}$ is significantly smaller than $\langle B_f^{\text{TTW}} \rangle_{s,t}$. Such discrepancy might be partially due to the arbitrarily imposed homogeneous boundary condition on w^{vm} at the lower bound of the computational domain.

We then compare $\langle B_f^{\text{vm}} \rangle_s$ to the estimate derived from the model proposed by Garrett and Loder (1981) (referred to as the GL81 model henceforth). The GL81 model can be treated as a simplification of TTW by neglecting the vertical mixing of ageostrophic flows. The vertical eddy buoyancy flux inferred from the GL81 model, $\langle B_f^{\text{GL81}} \rangle_s = \langle w^{\text{GL81}} b' \rangle_s$ with $w^{\text{GL81}} = -f^{-2} \nabla_H \cdot (K_m \nabla_H b)$, exhibits similar temporal variation to that of $\langle B_f^{\text{vm}} \rangle_s$. However, its magnitude is considerably larger (Figs. 11b,e), suggesting that the GL81 model severely overestimates the vertical eddy buoyancy flux contributed by $\langle B_f^{\text{vm}} \rangle_s$. To uncover the underlying reasons for the overestimation, we decompose the $\langle B_f^{\text{TTW}} \rangle_s$ into the following four terms:

$$\begin{aligned} \langle B_f^{\text{TTW}} \rangle_s = & \left\langle \frac{b'}{f \rho_0} \nabla_H \times \boldsymbol{\tau} \cdot \mathbf{k} \right\rangle_s - \frac{1}{A} \oint \frac{1}{f} b' K_m \frac{\partial \mathbf{v}}{\partial z} \cdot d\mathbf{l} \\ & + \left\langle K_m \frac{\partial \mathbf{v}_g}{\partial z} \cdot \frac{\partial \mathbf{v}_g}{\partial z} \right\rangle_s + \left\langle K_m \frac{\partial \mathbf{v}_a}{\partial z} \cdot \frac{\partial \mathbf{v}_g}{\partial z} \right\rangle_s, \end{aligned} \quad (20)$$

where A is the area of the computational domain and $d\mathbf{l}$ is the line element along the boundaries. To derive Eq. (20), we assume $\nabla_H b \approx \nabla_H b'$, an approximation of high-level of accuracy.

The first term on the rhs of Eq. (20) ($\langle B_{f,\text{tau}}^{\text{TTW}} \rangle_s$) represents the buoyancy flux related to the wind-induced Ekman pumping.

The second term ($\langle B_{f,\text{bry}}^{\text{TTW}} \rangle_s$) is the boundary effect that is found to be negligible. The third term ($\langle B_{f,\text{gs}}^{\text{TTW}} \rangle_s$), the destruction of geostrophic shear by vertical mixing, is positive definite. The last term ($\langle B_{f,\text{ags}}^{\text{TTW}} \rangle_s$), related to the dot product of geostrophic and ageostrophic shears, is found to be negative and largely cancel the contribution of $\langle B_{f,\text{gs}}^{\text{TTW}} \rangle_s$ to $\langle B_f^{\text{TTW}} \rangle_s$ (Figs. 11c,f). The negative correlation between geostrophic and ageostrophic shears can be understood based on the relationship of their surface values to wind stress, i.e., $\boldsymbol{\tau} = \rho_0 K_m (\partial \mathbf{v}_g / \partial z + \partial \mathbf{v}_a / \partial z)|_{z=0}$.⁵ It is found that the direction of wind stress is generally independent of that of $\partial \mathbf{v}_g / \partial z|_{z=0}$ (not shown) so that $\langle \boldsymbol{\tau} \cdot \partial \mathbf{v}_g / \partial z|_{z=0} \rangle_{s,t} = \langle \rho_0 K_m (\partial \mathbf{v}_g / \partial z + \partial \mathbf{v}_a / \partial z) \cdot \partial \mathbf{v}_g / \partial z|_{z=0} \rangle_{s,t}$ is close to zero. This leads to a strong cancellation between $\partial \mathbf{v}_g / \partial z$ and $\partial \mathbf{v}_a / \partial z$. The negligence of vertical mixing of ageostrophic flows by the GL81 model makes it incapable of representing the above effect and thus results in a severe overestimation of vertical eddy buoyancy flux.

5. Discussion

a. Implications

Ocean eddies, especially at submesoscales, cannot be resolved by the current generation of climate models and hence their important contribution to the vertical transport needs to be parameterized. So far only the parameterization for the contribution from mixed layer instability has been well proposed and implemented in climate models (Fox-Kemper and Ferrari 2008; Fox-Kemper et al. 2008, 2011). Yet analyses in this study suggest the important roles of frontogenesis/frontolysis and turbulent thermal winds as well in generating the vertical

⁵Strictly speaking, this equation should be applied to the level just below the surface where surface roughness elements and molecular processes become negligible.

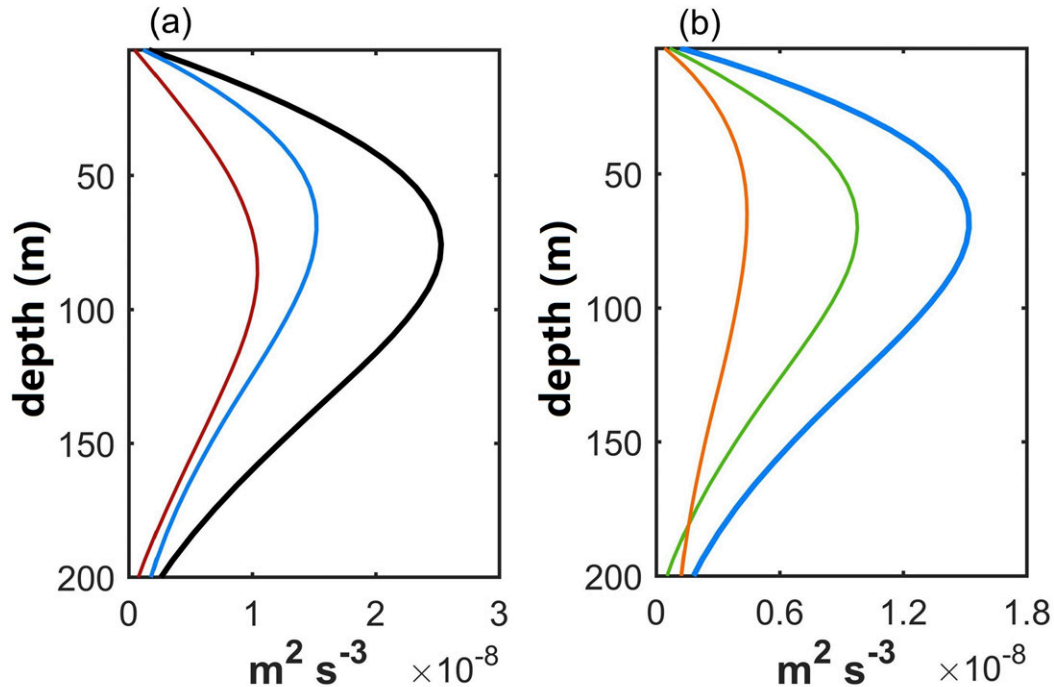


FIG. 10. (a) Decomposition of $\langle B_f^{qg} \rangle_{s,d}$ (black) into $\langle B_f^{FS} \rangle_{s,d}$ (blue) and $\langle B_f^{MLI} \rangle_{s,d}$ (red). (b) Decomposition of $\langle B_f^{FS} \rangle_{s,d}$ (blue) into contributions from the first term (green) and the second term (orange) on the rhs of Eq. (16).

eddy heat transport in the winter mixed layer of the Kuroshio Extension. We note that the significant ASCs induced by frontogenesis/frontolysis and turbulent thermal winds in this study are consistent with the recent findings obtained from observations (Zhang and Qiu 2018; Yu et al. 2019; Zhang et al. 2019; Siegelman et al. 2020) and high-resolution ocean general circulation models with realistic settings (Capet et al. 2008b; Gula et al. 2014; Qiu et al. 2016, 2020; Estrada-Allis et al. 2019). It thus implies inadequacies of existing parameterizations to represent the vertical eddy heat transport. Developing parameterizations for the vertical eddy heat transport from frontogenesis/frontolysis and turbulent thermal winds will be crucial for improvement in model representation and prediction of climate variability.

Observational studies usually neglect the effect of vertical mixing and assume a thermal wind balance for eddy motions partially due to the lack of concomitant mixing measurement (Martin and Richards 2001; Thomas and Joyce 2010; Pidcock et al. 2013; Thompson et al. 2016; Viglione et al. 2018; Siegelman et al. 2020). However, this study among others (e.g., Giordani et al. 2006; Nagai et al. 2006; Pallas-Sanz et al. 2010; Qiu et al. 2020) reveals the important role of vertical mixing of momentum in the eddy dynamics in the mixed layer. In particular, the results suggest that the turbulent thermal wind balance is a better representation of eddy motions than the thermal wind balance. It can be shown that the Ertel potential vorticity (PV), a key indicator used in stability analysis (Hoskins 1974; Haie and Marshall 1998; D'Asaro et al. 2011; Thomas et al. 2013; Thompson et al. 2016; Adams et al. 2017; Viglione et al. 2018),

computed by assuming a thermal wind balance has a significant negative (positive) bias in the northern (southern) hemisphere if the eddy motions are actually in turbulent thermal wind balance. In addition, given that the intensity of vertical mixing is strongly modulated by the surface heat flux and wind stress, the air–sea interactions may have a strong impact on the vertical eddy heat transport in the mixed layer. Such effects will be addressed in Part II (P. Yang et al. 2020, unpublished manuscript).

Most of the existing studies address the vertical eddy velocity. In particular, the SWOT satellite will be launched in 2021, increasing the resolution of SSH measurement from around 150 to 15 km (Fu et al. 2014). There are rising interests (e.g., Wang et al. 2013; Qiu et al. 2016, 2020; Liu et al. 2019) in reconstructing the vertical eddy velocities in the upper ocean based on the SWOT measurements. However, this study reveals the low-to-moderate spectral correlation between vertical eddy velocities and temperature anomalies, suggesting that a large portion of vertical eddy velocities are incapable of producing net vertical heat transport. Therefore, analyzing the vertical eddy velocity is not sufficient for estimating and understanding the vertical eddy heat transport. The reasons why the G-GMA omega equation can well reproduce the vertical eddy motions relevant to heat transport but less so for their irrelevant part deserves further investigation. It may help in gaining insight into interpretation and usage of SWOT measurements.

b. Limitations

We caution that the results are derived from a high-resolution numerical simulation and may not be fully applicable to the

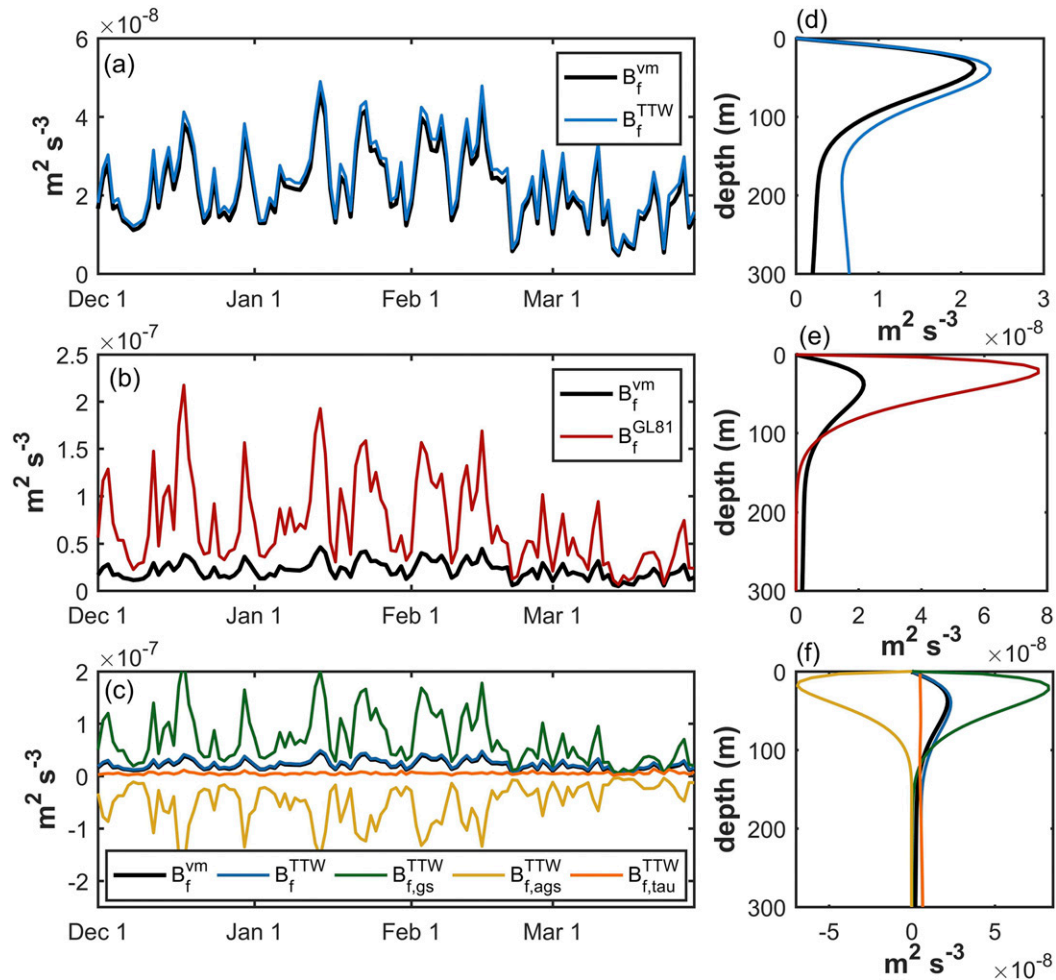


FIG. 11. Time series of (a) $\langle B_f^{vm} \rangle_s$ (black) and $\langle B_f^{TTW} \rangle_s$ (blue); (b) $\langle B_f^{GL81} \rangle_s$ (red); and (c) $\langle B_f^{TTW} \rangle_s$ (green), $\langle B_f^{GL81} \rangle_s$ (yellow), and $\langle B_f^{f,tau} \rangle_s$ (orange) at the peaking depth (40 m) of $\langle B_f^{vm} \rangle_s$. (d)–(f) Vertical profiles of time-mean variables shown in (a)–(c).

real ocean. There are several limitations in our simulation and analysis. First, the horizontal grid size is not fine enough to well resolve the symmetric instability (SI) (Stone 1966; Haine and Marshall 1998; D'Asaro et al. 2011). Indeed, the regional averaged bulk Richardson number in the mixed layer generally exceeds unity in our simulation (not shown), suggesting a minor or negligible role of SI in generating the vertical eddy heat transport. However, it does not necessarily mean that SI is unimportant in the Kuroshio Extension region but is probably a result of insufficient resolution. Second, it is difficult to separate the effects of frontogenesis/frontolysis and mixed layer instability as suggested by their similar parameterization forms for vertical eddy buoyancy flux (Fox-Kemper et al. 2008; McWilliams 2016). Specifically, the expression for frontogenesis/frontolysis induced vertical eddy buoyancy flux differs from Eq. (10) only by a factor proportional to $-(\partial \tilde{u}_{g,n}/\partial n)^2/f$. In this study, we tentatively isolate the effect of mixed layer instability from frontogenesis/frontolysis by searching samples with $-(\partial \tilde{u}_{g,n}/\partial n)^2/f = 0$. However, such an isolation neglects the interactions between these

two mechanisms (Boccaletti et al. 2007; McWilliams et al. 2009; Callies et al. 2016; McWilliams 2016). On one hand, sharpening/flattening the density fronts by frontogenesis/frontolysis can intensify/weaken mixed layer instability. On the other hand, the occurrence of mixed layer instability can destroy fronts that are essential ingredients for frontogenesis/frontolysis. Therefore, quantitative estimates for contributions from the mixed layer instability and net effect of frontogenesis/frontolysis to vertical eddy heat transport should be treated with caution. Finally, although the KPP scheme is widely used in simulations with comparable horizontal grid size to ours (Capet et al. 2008a; Rosso et al. 2014; Estrada-Allis et al. 2019), its validity has not been strictly justified in the presence of strong horizontal density gradients. A recent study by Mukherjee et al. (2016) found that the mixed-layer EKE budget simulated by models with 500-m horizontal grid size and KPP scheme is similar to that derived from large-eddy simulation. It thus suggests that the uncertainties in the KPP scheme are unlikely to change the results of this study qualitatively but some quantitative influences may exist.

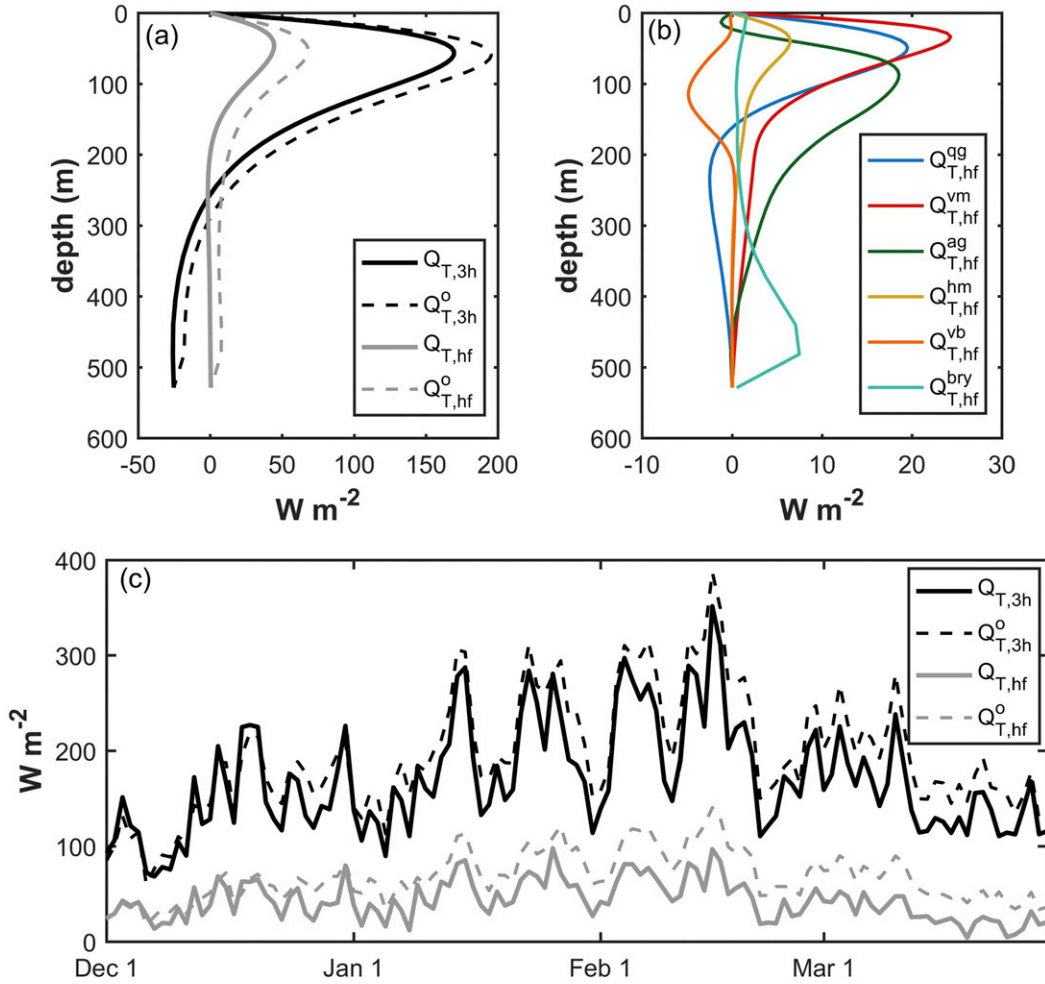


FIG. 12. (a) Vertical profiles of $\langle Q_{T,3h} \rangle_{s,t}$ (solid black), $\langle Q_{T,3h}^o \rangle_{s,t}$ (dashed black), $\langle Q_{T,hf} \rangle_{s,t}$ (solid gray), $\langle Q_{T,hf}^o \rangle_{s,t}$ (dashed gray). (b) Decomposition of $\langle Q_{T,hf}^o \rangle_{s,t}$ into different dynamical components following Eq. (9). (c) Time series of $\langle Q_{T,3h} \rangle_s$ (solid black), $\langle Q_{T,3h}^o \rangle_s$ (dashed black), $\langle Q_{T,hf} \rangle_s$ (solid gray), $\langle Q_{T,hf}^o \rangle_s$ (dashed gray) at 60 m where both $\langle Q_{T,3h} \rangle_{s,t}$ and $\langle Q_{T,hf} \rangle_{s,t}$ peak. Refer to main text for the meanings of symbols.

All variables used in this study are low-pass filtered with a cutoff frequency of $0.8f$ to remove interference from internal gravity waves. However, such a filter also damps the submesoscale eddy variabilities with time scales comparable to $1/f$ (Thomas et al. 2008; McWilliams 2016; Torres et al. 2018), making the computed vertical eddy heat transport bias low. Figure 12 compares the vertical eddy heat transport derived from the low-pass-filtered fields and that from the 3-hourly averaged model output (denoted as $Q_{T,3h}$) resolving processes with frequencies lower than $\sim 4f$. As expected, the vertical and temporal variations of $Q_{T,3h}$ and Q_T are similar to each other but the former's magnitude is systematically larger than that of the latter. At their peaking depth (~ 60 m), $\langle Q_T \rangle_{s,t}$ accounts for 75% of $\langle Q_{T,3h} \rangle_{s,t}$. We further examine the capability of G-GMA omega equation in reproducing $Q_{T,hf} = Q_{T,3h} - Q_T$ and find that it only shows moderate skills (Fig. 12). Although $Q_{T,hf}^o$ is able to capture the vertical and temporal variations

of $Q_{T,hf}$, its magnitude significantly biases high throughout the upper 500 m. The degraded performance of G-GMA omega equation in reproducing $Q_{T,hf}$ is understandable as internal gravity waves contained in the 3-hourly averaged variables are misrepresented by the GMA dynamics. Decomposition of $Q_{T,hf}^o$ into different dynamical components following Eq. (9) suggests that the ageostrophic advection becomes important and makes a similar contribution compared to the geostrophic deformation and the vertical mixing of momentum (Fig. 12b). However, given the significant uncertainties in $Q_{T,hf}^o$, it is unclear whether this important role of ageostrophic advection is reliable.

6. Conclusions

In this study, we explore the vertical eddy heat transport Q_T and its controlling dynamics in the winter Kuroshio Extension based on a 1-km regional simulation. An omega

equation with the geostrophic momentum approximation (GMA) and generalized to include viscous and diabatic effects (i.e., G-GMA omega equation) is proposed to decompose the contribution of Q_T from different dynamics. The major conclusions are summarized as follows:

- 1) The spectral correlation between vertical eddy velocities and temperature anomalies is less than 0.6 in the mixed layer, suggesting that not all vertical eddy motions make net contribution to the heat transport averaged over time and/or space. The G-GMA omega equation shows good skills in reproducing the magnitude of Q_T as well as its spatial and temporal variability but is less so for the vertical eddy velocity itself.
- 2) The simulated Q_T exhibits a pronounced positive peak around the center of the mixed layer (~ 60 m) and decays to zero around 250 m below which Q_T reverses its sign and exhibits a weak negative peak around 400 m. The value of Q_T within the mixed layer has multi-time-scale variations with irregularly occurring extreme events superimposed on a slowly varying seasonal cycle.
- 3) The geostrophic deformation and the vertical mixing of momentum are the two major processes accounting for Q_T in the mixed layer with the former and the latter generating positive peaks of Q_T around 75 and 40 m, respectively. The geostrophic deformation induced Q_T explains the seasonal variation of Q_T in the mixed layer, whereas Q_T produced by vertical mixing of momentum is largely responsible for those extreme events.

- 4) The geostrophic deformation induced Q_T results from the net effect of frontogenesis/frontolysis and mixed layer instability with the two mechanisms playing comparable roles. The contribution to Q_T from the vertical mixing of momentum can be accounted for by the turbulent thermal wind balance.

Acknowledgments. This research is supported by National Science Foundation of China (41822601, 41776006), Taishan Scholar Funds (tsqn201909052), and Transparent Ocean technology Innovation Project (2018SDKJ0102). The model simulation and many of the computations were executed at the High Performance Computing Center of Pilot National Laboratory for Marine Science and Technology (Qingdao). We would like to acknowledge supports from the International Laboratory for High-Resolution Earth System Prediction, a collaboration by Pilot National Laboratory for Marine Science and Technology, Texas A&M University, and the U.S. National Center for Atmospheric Research.

APPENDIX

Derivation of G-GMA Omega Equation

Taking $\partial/\partial z$ of Eq. (1) and $\partial/\partial y$ of Eq. (3), and using the thermal wind balance to eliminate the time derivative terms, we obtain

$$\begin{aligned} -f^2 \frac{\partial v_a}{\partial z} + \frac{\partial w}{\partial y} \frac{\partial b}{\partial z} - \frac{\partial w}{\partial z} \frac{\partial b}{\partial y} = & -2 \left(\frac{\partial u_g}{\partial y} \frac{\partial b}{\partial x} + \frac{\partial v_g}{\partial y} \frac{\partial b}{\partial y} \right) - f \left(\frac{\partial u_a}{\partial z} \frac{\partial u_g}{\partial x} + \frac{\partial v_a}{\partial z} \frac{\partial u_g}{\partial y} \right) \\ & - \left(\frac{\partial u_a}{\partial y} \frac{\partial b}{\partial x} + \frac{\partial v_a}{\partial y} \frac{\partial b}{\partial y} \right) + f \frac{\partial}{\partial z} [D_V(u) + D_H(u)] + \frac{\partial}{\partial y} [D_V(b)]. \end{aligned} \quad (A1)$$

Replacing $-(\partial w/\partial z)(\partial b/\partial y)$ with $(\partial u_a/\partial x + \partial v_a/\partial y)(\partial b/\partial y)$, Eq. (A1) is re-expressed as

$$\begin{aligned} -f^2 \frac{\partial v_a}{\partial z} + \frac{\partial w}{\partial y} \frac{\partial b}{\partial z} = & -2 \left(\frac{\partial u_g}{\partial y} \frac{\partial b}{\partial x} + \frac{\partial v_g}{\partial y} \frac{\partial b}{\partial y} \right) - f \left(\frac{\partial u_a}{\partial z} \frac{\partial u_g}{\partial x} + \frac{\partial v_a}{\partial z} \frac{\partial u_g}{\partial y} \right) \\ & - \left(\frac{\partial u_a}{\partial y} \frac{\partial b}{\partial x} + 2 \frac{\partial v_a}{\partial y} \frac{\partial b}{\partial y} + \frac{\partial u_a}{\partial x} \frac{\partial b}{\partial y} \right) + f \frac{\partial}{\partial z} [D_V(u) + D_H(u)] + \frac{\partial}{\partial y} [D_V(b)]. \end{aligned} \quad (A2)$$

Applying similar manipulations to Eqs. (2) and (3) yields

$$\begin{aligned} -f^2 \frac{\partial u_a}{\partial z} + \frac{\partial w}{\partial x} \frac{\partial b}{\partial z} = & -2 \left(\frac{\partial u_g}{\partial x} \frac{\partial b}{\partial x} + \frac{\partial v_g}{\partial x} \frac{\partial b}{\partial y} \right) + f \left(\frac{\partial u_a}{\partial z} \frac{\partial v_g}{\partial x} + \frac{\partial v_a}{\partial z} \frac{\partial v_g}{\partial y} \right) \\ & - \left(2 \frac{\partial u_a}{\partial x} \frac{\partial b}{\partial x} + \frac{\partial v_a}{\partial x} \frac{\partial b}{\partial y} + \frac{\partial v_a}{\partial y} \frac{\partial b}{\partial x} \right) - f \frac{\partial}{\partial z} [D_V(v) + D_H(v)] + \frac{\partial}{\partial x} [D_V(b)]. \end{aligned} \quad (A3)$$

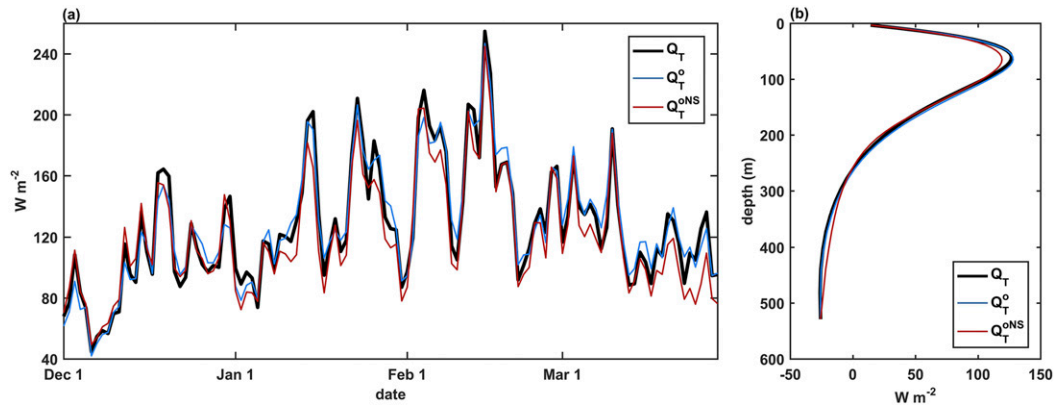


FIG. A1. (a) Time series of $\langle Q_T \rangle_s$ (black), $\langle Q_T^o \rangle_s$ (blue), and $\langle Q_T^{oNS} \rangle_s$ (red) at 60 m. (b) Vertical profiles of time-mean variables shown in (a).

Taking $\partial/\partial y$ of Eq. (A2) and $\partial/\partial x$ of Eq. (A3) and adding them together leads to Eqs. (5)–(7).

The vertical eddy heat transport derived from the solution of Eq. (5) (Q_T^{oNS}) is similar to that of Q_T^o in both the vertical distribution and the temporal variation (Fig. A1).

REFERENCES

- Adams, K. A., P. Hosegood, J. R. Taylor, J.-B. Sallée, S. Bachman, R. Torres, and M. Stamper, 2017: Frontal circulation and submesoscale variability during the formation of a Southern Ocean mesoscale eddy. *J. Phys. Oceanogr.*, **47**, 1737–1753, <https://doi.org/10.1175/JPO-D-16-0266.1>.
- Alford, M. H., J. A. MacKinnon, H. L. Simmons, and J. D. Nash, 2016: Near-inertial internal gravity waves in the ocean. *Annu. Rev. Mar. Sci.*, **8**, 95–123, <https://doi.org/10.1146/annurev-marine-010814-015746>.
- Allen, J. T., D. A. Smeed, A. J. G. Nurser, J. W. Zhang, and M. Rixen, 2001: Diagnosis of vertical velocities with the QG omega equation: An examination of the errors due to sampling strategy. *Deep-Sea Res. I*, **48**, 315–346, [https://doi.org/10.1016/S0967-0637\(00\)00035-2](https://doi.org/10.1016/S0967-0637(00)00035-2).
- Bachman, S. D., and J. R. Taylor, 2016: Numerical simulations of the equilibrium between eddy-induced restratification and vertical mixing. *J. Phys. Oceanogr.*, **46**, 919–935, <https://doi.org/10.1175/JPO-D-15-0110.1>.
- Boccaletti, G., R. Ferrari, and B. Fox-Kemper, 2007: Mixed layer instabilities and restratification. *J. Phys. Oceanogr.*, **37**, 2228–2250, <https://doi.org/10.1175/JPO3101.1>.
- Callies, J., and R. Ferrari, 2018a: Baroclinic instability in the presence of convection. *J. Phys. Oceanogr.*, **48**, 45–60, <https://doi.org/10.1175/JPO-D-17-0028.1>.
- , and —, 2018b: Note on the rate of restratification in the baroclinic spin-down of fronts. *J. Phys. Oceanogr.*, **48**, 1543–1553, <https://doi.org/10.1175/JPO-D-17-0175.1>.
- , —, J. M. Klymak, and J. Gula, 2015: Seasonality in submesoscale turbulence. *Nat. Commun.*, **6**, 6862, <https://doi.org/10.1038/ncomms7862>.
- , G. Flierl, R. Ferrari, and B. Fox-Kemper, 2016: The role of mixed-layer instabilities in submesoscale turbulence. *J. Fluid Mech.*, **788**, 5–41, <https://doi.org/10.1017/jfm.2015.700>.
- Capet, X., J. C. McWilliams, M. J. Molemaker, and A. F. Shchepetkin, 2008a: Mesoscale to submesoscale transition in the California Current system. Part I: Flow structure, eddy flux, and observational tests. *J. Phys. Oceanogr.*, **38**, 29–43, <https://doi.org/10.1175/2007JPO3671.1>.
- , —, —, and —, 2008b: Mesoscale to submesoscale transition in the California Current system. Part II: Frontal processes. *J. Phys. Oceanogr.*, **38**, 44–64, <https://doi.org/10.1175/2007JPO3672.1>.
- , G. Roullet, P. Klein, and G. Maze, 2016: Intensification of upper-ocean submesoscale turbulence through Charney baroclinic instability. *J. Phys. Oceanogr.*, **46**, 3365–3384, <https://doi.org/10.1175/JPO-D-16-0050.1>.
- Carton, J. A., G. A. Chepurin, and L. Chen, 2018: SODA3: A new ocean climate reanalysis. *J. Climate*, **31**, 6967–6983, <https://doi.org/10.1175/JCLI-D-18-0149.1>.
- Chelton, D. B., M. G. Schlax, M. H. Freilich, and R. F. Milliff, 2004: Satellite measurements reveal persistent small-scale features in ocean winds. *Science*, **303**, 978–983, <https://doi.org/10.1126/science.1091901>.
- Chen, R., G. R. Flierl, and C. Wunsch, 2014: A description of local and nonlocal eddy-mean flow interaction in a global eddy-permitting state estimate. *J. Phys. Oceanogr.*, **44**, 2336–2352, <https://doi.org/10.1175/JPO-D-14-0009.1>.
- Cloke, P., and M. J. P. Cullen, 1994: A semi-geostrophic ocean model with outcropping. *Dyn. Atmos. Oceans*, **21**, 23–48, [https://doi.org/10.1016/0377-0265\(94\)90024-8](https://doi.org/10.1016/0377-0265(94)90024-8).
- Cronin, M. F., and Coauthors, 2010: Monitoring ocean-atmosphere interactions in western boundary current extensions. *Proceedings of OceanObs'09: Sustained Ocean Observations and Information for Society*, Vol. 2, J. Hall, D. E. Harrison, and D. Stammer, Eds., ESA Publication WPP-306, European Space Agency, 199–209, <https://doi.org/10.5270/OceanObs09.cwp.20>.
- D'Asaro, E., C. Lee, L. Rainville, R. Harcourt, and L. Thomas, 2011: Enhanced turbulence and energy dissipation at ocean fronts. *Science*, **332**, 318–322, <https://doi.org/10.1126/science.1201515>.
- Ducet, N., and P.-Y. Le Traon, 2001: A comparison of surface eddy kinetic energy and Reynolds stresses in the Gulf Stream and the Kuroshio Current systems from merged TOPEX/Poseidon and ERS-1/2 altimetric data. *J. Geophys. Res.*, **106**, 16 603–16 622, <https://doi.org/10.1029/2000JC000205>.
- Eliassen, A., 1949: The quasi-static equations of motion with pressure as independent variable. *Geophys. Publ.*, **17**, 1–44.
- Estrada-Alis, S. N., B. Barceló-Llull, E. Pallàs-Sanz, A. Rodríguez-Santana, J. M. A. C. Souza, E. Mason, J. C. McWilliams, and P. Sangrà, 2019: Vertical velocity dynamics and mixing in an anticyclone near the canary islands. *J. Phys. Oceanogr.*, **49**, 431–451, <https://doi.org/10.1175/JPO-D-17-0156.1>.

- Ferrari, R., and C. Wunsch, 2009: Ocean circulation kinetic energy: Reservoirs, sources, and sinks. *Annu. Rev. Fluid Mech.*, **41**, 253–282, <https://doi.org/10.1146/annurev.fluid.40.111406.102139>.
- Fox-Kemper, B., and R. Ferrari, 2008: Parameterization of mixed layer eddies. Part II: Prognosis and impact. *J. Phys. Oceanogr.*, **38**, 1166–1179, <https://doi.org/10.1175/2007JPO3788.1>.
- , —, and R. Hallberg, 2008: Parameterization of mixed layer eddies. Part I: Theory and diagnosis. *J. Phys. Oceanogr.*, **38**, 1145–1165, <https://doi.org/10.1175/2007JPO3792.1>.
- , and Coauthors, 2011: Parameterization of mixed layer eddies. III: Implementation and impact in global ocean climate simulations. *Ocean Modell.*, **39**, 61–78, <https://doi.org/10.1016/j.ocemod.2010.09.002>.
- Fu, L.-L., and C. Ubelmann, 2014: On the transition from profile altimeter to swath altimeter for observing global ocean surface topography. *J. Atmos. Oceanic Technol.*, **31**, 560–568, <https://doi.org/10.1175/JTECH-D-13-00109.1>.
- Garrett, C. J. R., and J. W. Loder, 1981: Dynamical aspects of shallow sea fronts. *Philos. Trans. Roy. Soc. London*, **302A**, 563–581, <https://doi.org/10.1098/rsta.1981.0183>.
- Giordani, H., and S. Planton, 2000: Modeling and analysis of ageostrophic circulation over the Azores oceanic front during the SEMAPHORE experiment. *Mon. Wea. Rev.*, **128**, 2270–2287, [https://doi.org/10.1175/1520-0493\(2000\)128<2270:MAAOAC>2.0.CO;2](https://doi.org/10.1175/1520-0493(2000)128<2270:MAAOAC>2.0.CO;2).
- , L. Prieur, and G. Caniaux, 2006: Advanced insights into sources of vertical velocity in the ocean. *Ocean Dyn.*, **56**, 513–524, <https://doi.org/10.1007/s10236-005-0050-1>.
- Griffies, S. M., and R. W. Hallberg, 2000: Biharmonic friction with a Smagorinsky-like viscosity for use in large-scale eddy-permitting ocean models. *Mon. Wea. Rev.*, **128**, 2935–2946, [https://doi.org/10.1175/1520-0493\(2000\)128<2935:BFWASL>2.0.CO;2](https://doi.org/10.1175/1520-0493(2000)128<2935:BFWASL>2.0.CO;2).
- Gula, J., M. J. Molemaker, and J. C. McWilliams, 2014: Submesoscale cold filaments in the Gulf Stream. *J. Phys. Oceanogr.*, **44**, 2617–2643, <https://doi.org/10.1175/JPO-D-14-0029.1>.
- Haidvogel, D. B., H. G. Arango, K. Hedstrom, A. Beckmann, P. Malanotte-Rizzoli, and A. F. Shchepetkin, 2000: Model evaluation experiments in the North Atlantic Basin: Simulations in nonlinear terrain-following coordinates. *Dyn. Atmos. Oceans*, **32**, 239–281, [https://doi.org/10.1016/S0377-0265\(00\)00049-X](https://doi.org/10.1016/S0377-0265(00)00049-X).
- Haine, T. W. N., and J. Marshall, 1998: Gravitational, symmetric, and baroclinic instability of the ocean mixed layer. *J. Phys. Oceanogr.*, **28**, 634–658, [https://doi.org/10.1175/1520-0485\(1998\)028<0634:GSABIO>2.0.CO;2](https://doi.org/10.1175/1520-0485(1998)028<0634:GSABIO>2.0.CO;2).
- Hoskins, B. J., 1974: The role of potential vorticity in symmetric stability and instability. *Quart. J. Roy. Meteor. Soc.*, **100**, 480–482, <https://doi.org/10.1002/qj.49710042520>.
- , 1975: The geostrophic momentum approximation and the semi-geostrophic equations. *J. Atmos. Sci.*, **32**, 233–242, [https://doi.org/10.1175/1520-0469\(1975\)032<0233:TGMAAT>2.0.CO;2](https://doi.org/10.1175/1520-0469(1975)032<0233:TGMAAT>2.0.CO;2).
- , 1982: The mathematical theory of frontogenesis. *Annu. Rev. Fluid Mech.*, **14**, 131–151, <https://doi.org/10.1146/annurev.fl.14.010182.001023>.
- , and F. P. Bretherton, 1972: Atmospheric frontogenesis models: Mathematical formulation and solution. *J. Atmos. Sci.*, **29**, 11–37, [https://doi.org/10.1175/1520-0469\(1972\)029<0011:AFMMFA>2.0.CO;2](https://doi.org/10.1175/1520-0469(1972)029<0011:AFMMFA>2.0.CO;2).
- Jing, Z., and Coauthors, 2020: Maintenance of mid-latitude oceanic fronts by mesoscale eddies. *Sci. Adv.*, **6**, eaba7880, <https://doi.org/10.1126/sciadv.aba7880>.
- Klein, P., and G. Lapeyre, 2009: The oceanic vertical pump induced by mesoscale and submesoscale turbulence. *Annu. Rev. Mar. Sci.*, **1**, 351–375, <https://doi.org/10.1146/annurev.marine.010908.163704>.
- Lapeyre, G., and P. Klein, 2006: Dynamics of the upper oceanic layers in terms of surface quasigeostrophy theory. *J. Phys. Oceanogr.*, **36**, 165–176, <https://doi.org/10.1175/JPO2840.1>.
- Large, W. G., J. C. McWilliams, and S. C. Doney, 1994: Oceanic vertical mixing: A review and a model with a nonlocal boundary layer parameterization. *Rev. Geophys.*, **32**, 363–403, <https://doi.org/10.1029/94RG01872>.
- Liu, L., H. Xue, and H. Sasaki, 2019: Reconstructing the ocean interior from high-resolution sea surface information. *J. Phys. Oceanogr.*, **49**, 3245–3262, <https://doi.org/10.1175/JPO-D-19-0118.1>.
- Mahadevan, A., and A. Tandon, 2006: An analysis of mechanisms for submesoscale vertical motion at ocean fronts. *Ocean Modell.*, **14**, 241–256, <https://doi.org/10.1016/j.ocemod.2006.05.006>.
- , E. D’Asaro, C. Lee, and M. J. Perry, 2012: Eddy-driven stratification initiates North Atlantic spring phytoplankton blooms. *Science*, **337**, 54–58, <https://doi.org/10.1126/science.1218740>.
- Martin, A. P., and K. J. Richards, 2001: Mechanisms for vertical nutrient transport within a North Atlantic mesoscale eddy. *Deep-Sea Res. II*, **48**, 757–773, [https://doi.org/10.1016/S0967-0645\(00\)00096-5](https://doi.org/10.1016/S0967-0645(00)00096-5).
- McGillicuddy, D. J., L. A. Anderson, S. C. Doney, and M. E. Maltrud, 2003: Eddy-driven sources and sinks of nutrients in the upper ocean: Results from a 0.1° resolution model of the North Atlantic. *Global Biogeochem. Cycles*, **17**, 1035, <https://doi.org/10.1029/2002GB001987>.
- McWilliams, J. C., 2016: Submesoscale currents in the ocean. *Proc. Roy. Soc.*, **472A**, 20160117, <https://doi.org/10.1098/rspa.2016.0117>.
- , M. J. Molemaker, and E. I. Olafsdottir, 2009: Linear fluctuation growth during frontogenesis. *J. Phys. Oceanogr.*, **39**, 3111–3129, <https://doi.org/10.1175/2009JPO4186.1>.
- Mensa, J. A., Z. Garraffo, A. Griffa, T. M. Özgökmen, A. Haza, and M. Veneziani, 2013: Seasonality of the submesoscale dynamics in the Gulf Stream region. *Ocean Dyn.*, **63**, 923–941, <https://doi.org/10.1007/s10236-013-0633-1>.
- Minobe, S., A. Kuwano-Yoshida, N. Komori, S.-P. Xie, and R. J. Small, 2008: Influence of the Gulf Stream on the troposphere. *Nature*, **452**, 206–209, <https://doi.org/10.1038/nature06690>.
- Mukherjee, S., S. Ramachandran, A. Tandon, and A. Mahadevan, 2016: Production and destruction of eddy kinetic energy in forced submesoscale eddy-resolving simulations. *Ocean Modell.*, **105**, 44–59, <https://doi.org/10.1016/j.ocemod.2016.07.002>.
- Nagai, T., A. Tandon, and D. L. Rudnick, 2006: Two-dimensional ageostrophic secondary circulation at ocean fronts due to vertical mixing and large-scale deformation. *J. Geophys. Res.*, **111**, C09038, <https://doi.org/10.1029/2005JC002964>.
- Nakamura, H., T. Sampe, A. Goto, W. Ohfuchi, and S.-P. Xie, 2008: On the importance of midlatitude oceanic frontal zones for the mean state and dominant variability in the tropospheric circulation. *Geophys. Res. Lett.*, **35**, L15709, <https://doi.org/10.1029/2008GL034010>.
- Naveira Garabato, A. C., H. Leach, J. T. Allen, R. T. Pollard, and V. H. Strass, 2001: Mesoscale subduction at the Antarctic polar front driven by baroclinic instability. *J. Phys. Oceanogr.*, **31**, 2087–2107, [https://doi.org/10.1175/1520-0485\(2001\)031<2087:MSATAP>2.0.CO;2](https://doi.org/10.1175/1520-0485(2001)031<2087:MSATAP>2.0.CO;2).
- Pallàs-Sanz, E., and Á. Viúdez, 2005: Diagnosing mesoscale vertical motion from horizontal velocity and density data. *J. Phys. Oceanogr.*, **35**, 1744–1762, <https://doi.org/10.1175/JPO2784.1>.

- , T. M. S. Johnston, and D. L. Rudnick, 2010: Frontal dynamics in a California Current system shallow front: 2. Mesoscale vertical velocity. *J. Geophys. Res.*, **115**, C12068, <https://doi.org/10.1029/2010JC006474>.
- Pidcock, R., A. Martin, J. Allen, S. C. Painter, and D. Smeed, 2013: The spatial variability of vertical velocity in an Iceland basin eddy dipole. *Deep-Sea Res. I*, **72**, 121–140, <https://doi.org/10.1016/j.dsr.2012.10.008>.
- Pinot, J.-M., J. Tintoré, and D.-P. Wang, 1996: A study of the omega equation for diagnosing vertical motions at ocean fronts. *J. Mar. Res.*, **54**, 239–259, <https://doi.org/10.1357/0022240963213358>.
- Pollard, R. T., and L. A. Regier, 1992: Vorticity and vertical circulation at an ocean front. *J. Phys. Oceanogr.*, **22**, 609–625, [https://doi.org/10.1175/1520-0485\(1992\)022<0609:VAVCAA>2.0.CO;2](https://doi.org/10.1175/1520-0485(1992)022<0609:VAVCAA>2.0.CO;2).
- Press, W. H., S. A. Teukolsky, B. P. Flannery, and W. T. Vetterling, 1992: *Numerical Recipes in Fortran 77: The Art of Scientific Computing*. Cambridge University Press, 973 pp.
- Qiu, B., S. Chen, P. Klein, C. Uebelmann, L.-L. Fu, and H. Sasaki, 2016: Reconstructability of three-dimensional upper-ocean circulation from SWOT sea surface height measurements. *J. Phys. Oceanogr.*, **46**, 947–963, <https://doi.org/10.1175/JPO-D-15-0188.1>.
- , —, —, H. Torres, J. Wang, L.-L. Fu, and D. Menemenlis, 2020: Reconstructing upper-ocean vertical velocity field from sea surface height in the presence of unbalanced motion. *J. Phys. Oceanogr.*, **50**, 55–79, <https://doi.org/10.1175/JPO-D-19-0172.1>.
- Ramachandran, S., A. Tandon, and A. Mahadevan, 2014: Enhancement in vertical fluxes at a front by mesoscale-submesoscale coupling. *J. Geophys. Res. Oceans*, **119**, 8495–8511, <https://doi.org/10.1002/2014JC010211>.
- Rosso, L., A. McC. Hogg, P. G. Strutton, A. E. Kiss, R. Matear, A. Klocker, and E. van Sebille, 2014: Vertical transport in the ocean due to sub-mesoscale structures: Impacts in the Kerguelen region. *Ocean Modell.*, **80**, 10–23, <https://doi.org/10.1016/j.ocemod.2014.05.001>.
- Rudnick, D. L., 2001: On the skewness of vorticity in the upper ocean. *Geophys. Res. Lett.*, **28**, 2045–2048, <https://doi.org/10.1029/2000GL012265>.
- Saha, S., and Coauthors, 2010: The NCEP Climate Forecast System Reanalysis. *Bull. Amer. Meteor. Soc.*, **91**, 1015–1058, <https://doi.org/10.1175/2010BAMS3001.1>.
- Salmon, R., 1980: Baroclinic instability and geostrophic turbulence. *Geophys. Astrophys. Fluid Dyn.*, **15**, 167–211, <https://doi.org/10.1080/03091928008241178>.
- Shchepetkin, A. F., and J. C. McWilliams, 2005: The Regional Oceanic Modeling System (ROMS): A split-explicit, free-surface, topography-following-coordinate oceanic model. *Ocean Modell.*, **9**, 347–404, <https://doi.org/10.1016/j.ocemod.2004.08.002>.
- Shcherbina, A. Y., E. A. D'Asaro, C. M. Lee, J. M. Klymak, M. J. Molemaker, and J. C. McWilliams, 2013: Statistics of vertical vorticity, divergence, and strain in a developed submesoscale turbulence field. *Geophys. Res. Lett.*, **40**, 4706–4711, <https://doi.org/10.1002/grl.50919>.
- Siegelman, L., P. Klein, P. Rivière, A. F. Thompson, H. S. Torres, M. Flexas, and D. Menemenlis, 2020: Enhanced upward heat transport at deep submesoscale ocean fronts. *Nat. Geosci.*, **13**, 50–55, <https://doi.org/10.1038/s41561-019-0489-1>.
- Small, R. J., and Coauthors, 2008: Air–sea interaction over ocean fronts and eddies. *Dyn. Atmos. Oceans*, **45**, 274–319, <https://doi.org/10.1016/j.dynatmoce.2008.01.001>.
- Stone, P. H., 1966: On non-geostrophic baroclinic stability. *J. Atmos. Sci.*, **23**, 390–400, [https://doi.org/10.1175/1520-0469\(1966\)023<0390:ONGBS>2.0.CO;2](https://doi.org/10.1175/1520-0469(1966)023<0390:ONGBS>2.0.CO;2).
- , 1970: On non-geostrophic baroclinic stability: Part II. *J. Atmos. Sci.*, **27**, 721–726, [https://doi.org/10.1175/1520-0469\(1970\)027<0721:ONGBSP>2.0.CO;2](https://doi.org/10.1175/1520-0469(1970)027<0721:ONGBSP>2.0.CO;2).
- Su, Z., J. Wang, P. Klein, A. F. Thompson, and D. Menemenlis, 2018: Ocean submesoscales as a key component of the global heat budget. *Nat. Commun.*, **9**, 775, <https://doi.org/10.1038/s41467-018-02983-w>.
- Thomas, L. N., and C. M. Lee, 2005: Intensification of ocean fronts by down-front winds. *J. Phys. Oceanogr.*, **35**, 1086–1102, <https://doi.org/10.1175/JPO2737.1>.
- , and R. Ferrari, 2008: Friction, frontogenesis, and the stratification of the surface mixed layer. *J. Phys. Oceanogr.*, **38**, 2501–2518, <https://doi.org/10.1175/2008JPO3797.1>.
- , and T. M. Joyce, 2010: Subduction on the northern and southern flanks of the Gulf Stream. *J. Phys. Oceanogr.*, **40**, 429–438, <https://doi.org/10.1175/2009JPO4187.1>.
- , A. Tandon, and A. Mahadevan, 2008: Submesoscale processes and dynamics. *Ocean Modeling in an Eddying Regime*, *Geophys. Monogr.*, Vol. 177, Amer. Geophys. Union, 17–38, <https://doi.org/10.1029/177GM04>.
- , J. R. Taylor, R. Ferrari, and T. M. Joyce, 2013: Symmetric instability in the Gulf Stream. *Deep-Sea Res. II*, **91**, 96–110, <https://doi.org/10.1016/j.dsr2.2013.02.025>.
- Thompson, A. F., A. Lazar, C. Buckingham, A. C. Naveira Garabato, G. M. Damerell, and K. J. Heywood, 2016: Open-ocean submesoscale motions: A full seasonal cycle of mixed layer instabilities from Gliders. *J. Phys. Oceanogr.*, **46**, 1285–1307, <https://doi.org/10.1175/JPO-D-15-0170.1>.
- Tokinaga, H., Y. Tanimoto, S.-P. Xie, T. Sampe, H. Tomita, and H. Ichikawa, 2009: Ocean frontal effects on the vertical development of clouds over the western North Pacific: In situ and satellite observations. *J. Climate*, **22**, 4241–4260, <https://doi.org/10.1175/2009JCLI2763.1>.
- Torres, H. S., P. Klein, D. Menemenlis, B. Qiu, Z. Su, J. Wang, S. Chen, and L.-L. Fu, 2018: Partitioning ocean motions into balanced motions and internal gravity waves: A modeling study in anticipation of future space missions. *J. Geophys. Res. Oceans*, **123**, 8084–8105, <https://doi.org/10.1029/2018JC014438>.
- Viglione, G. A., A. F. Thompson, M. M. Flexas, J. Sprintall, and S. Swart, 2018: Abrupt transitions in submesoscale structure in southern drake passage: Glider observations and model results. *J. Phys. Oceanogr.*, **48**, 2011–2027, <https://doi.org/10.1175/JPO-D-17-0192.1>.
- Viúdez, Á., 2004: Potential vorticity and the quasigeostrophic and semigeostrophic mesoscale vertical velocity. *J. Phys. Oceanogr.*, **34**, 865–887, [https://doi.org/10.1175/1520-0485\(2004\)034<0865:PVATQA>2.0.CO;2](https://doi.org/10.1175/1520-0485(2004)034<0865:PVATQA>2.0.CO;2).
- von Storch, J.-S., C. Eden, I. Fast, H. Haak, D. Hernández-Deckers, E. Maier-Reimer, J. Marotzke, and D. Stammer, 2012: An estimate of the Lorenz energy cycle for the world ocean based on the STORM/NCEP simulation. *J. Phys. Oceanogr.*, **42**, 2185–2205, <https://doi.org/10.1175/JPO-D-12-079.1>.
- Wang, J., G. R. Flierl, J. H. LaCasce, J. L. McClean, and A. Mahadevan, 2013: Reconstructing the ocean's interior from surface data. *J. Phys. Oceanogr.*, **43**, 1611–1626, <https://doi.org/10.1175/JPO-D-12-0204.1>.
- Waterman, S., and S. R. Jayne, 2011: Eddy-mean flow interactions in the along-stream development of a western boundary

- current jet: An idealized model study. *J. Phys. Oceanogr.*, **41**, 682–707, <https://doi.org/10.1175/2010JPO4477.1>.
- Yu, L., and R. A. Weller, 2007: Objectively analyzed air–sea heat fluxes for the global ice-free oceans (1981–2005). *Bull. Amer. Meteor. Soc.*, **88**, 527–540, <https://doi.org/10.1175/BAMS-88-4-527>.
- Yu, X., A. C. Naveira Garabato, A. P. Martin, C. E. Buckingham, L. Brannigan, and Z. Su, 2019: An annual cycle of submesoscale vertical flow and restratification in the upper ocean. *J. Phys. Oceanogr.*, **49**, 1439–1461, <https://doi.org/10.1175/JPO-D-18-0253.1>.
- Zhang, Z., and B. Qiu, 2018: Evolution of submesoscale ageostrophic motions through the life cycle of oceanic mesoscale eddies. *Geophys. Res. Lett.*, **45**, 11 847–11 855, <https://doi.org/10.1029/2018GL080399>.
- , —, P. Klein, and S. Travis, 2019: The influence of geostrophic strain on oceanic ageostrophic motion and surface chlorophyll. *Nat. Commun.*, **10**, 2838, <https://doi.org/10.1038/s41467-019-10883-w>.
- Zhong, Y., and A. Bracco, 2013: Submesoscale impacts on horizontal and vertical transport in the Gulf of Mexico. *J. Geophys. Res. Oceans*, **118**, 5651–5668, <https://doi.org/10.1002/jgrc.20402>.